Review Article

Neuroimaging at 7 Tesla: a pictorial narrative review

Tomohisa Okada[1]^, Koji Fujimoto[2]^, Yasutaka Fushimi[3]^, Thai Akasaka[1]^, Dinh H. D. Thuy[1], Atsushi Shima[1]^, Nobukatsu Sawamoto[4]^, Naoya Oishi[5], Zhilin Zhang[6], Takeshi Funaki[7]^, Yuji Nakamoto[3]^, Toshiya Murai[6], Susumu Miyamoto[7]^, Ryosuke Takahashi[8]^, Tadashi Isa[1]^

[1]Human Brain Research Center, Graduate School of Medicine, Kyoto University, Kyoto, Japan; [2]Department of Real World Data Research and Development, Graduate School of Medicine, Kyoto University, Kyoto, Japan; [3]Department of Diagnostic Imaging and Nuclear Medicine, Graduate School of Medicine, Kyoto University, Kyoto, Japan; [4]Department of Human Health Sciences, Graduate School of Medicine, Kyoto University, Kyoto, Japan; [5]Medial Innovation Center, Graduate School of Medicine, Kyoto University, Kyoto, Japan; [6]Department of Psychiatry, Graduate School of Medicine, Kyoto University, Kyoto, Japan; [7]Department of Neurosurgery, Graduate School of Medicine, Kyoto University, Kyoto, Japan; [8]Department of Neurology, Graduate School of Medicine, Kyoto University, Kyoto, Japan

Contributions: (I) Conception and design: T Okada; (II) Administrative support: Y Nakamoto, T Murai, S Miyamoto, R Takahashi, T Isa; (III) Provision of study materials or patients: Y Fushimi, A Shima, N Sawamoto, N Oishi, Z Zhang, T Funaki, Y Nakamoto, T Murai, S Miyamoto, R Takahashi; (IV) Collection and assembly of data: T Okada, K Fujimoto, Y Fushimi, T Akasaka, DHD Thuy, A Shima, N Sawamoto, N Oishi, Z Zhang, T Funaki; (V) Data analysis and interpretation: T Okada, K Fujimoto, Y Fushimi, T Akasaka, A Shima, N Oishi, Z Zhang; (VI) Manuscript writing: All authors; (VII) Final approval of manuscript: All authors.

Correspondence to: Tomohisa Okada. Human Brain Research Center, 54 Shogoin Kawaharacho, Sakyoku, Kyoto 606-8507, Japan.
Email: tomokada@kuhp.kyoto-u.ac.jp.

Abstract: Neuroimaging using the 7-Tesla (7T) human magnetic resonance (MR) system is rapidly gaining popularity after being approved for clinical use in the European Union and the USA. This trend is the same for functional MR imaging (MRI). The primary advantages of 7T over lower magnetic fields are its higher signal-to-noise and contrast-to-noise ratios, which provide high-resolution acquisitions and better contrast, making it easier to detect lesions and structural changes in brain disorders. Another advantage is the capability to measure a greater number of neurochemicals by virtue of the increased spectral resolution. Many structural and functional studies using 7T have been conducted to visualize details in the white matter and layers of the cortex and hippocampus, the subnucleus or regions of the putamen, the globus pallidus, thalamus and substantia nigra, and in small structures, such as the subthalamic nucleus, habenula, perforating arteries, and the perivascular space, that are difficult to observe at lower magnetic field strengths. The target disorders for 7T neuroimaging range from tumoral diseases to vascular, neurodegenerative, and psychiatric disorders, including Alzheimer's disease, Parkinson's disease, multiple sclerosis, epilepsy, major depressive disorder, and schizophrenia. MR spectroscopy has also been used for research because of its increased chemical shift that separates overlapping peaks and resolves neurochemicals more effectively at 7T than a lower magnetic field. This paper presents a narrative review of these topics and an illustrative presentation of images obtained at 7T. We expect 7T neuroimaging to provide a new imaging biomarker of various brain disorders.

Keywords: 7 Tesla (7T); MP2RAGE; susceptibility; functional magnetic resonance imaging (fMRI); magnetic resonance spectroscopy (MRS)

^ ORCID: Tomohisa Okada, 0000-0003-2312-5677; Koji Fujimoto, 0000-0003-1209-7949; Yasutaka Fushimi, 0000-0002-1982-3168; Thai Akasaka, 0000-0002-6602-5732; Atsushi Shima, 0000-0002-3068-4621; Nobukatsu Sawamoto, 0000-0001-8695-0223; Takeshi Funaki, 0000-0001-9489-7469; Yuji Nakamoto, 0000-0001-5783-8048; Susumu Miyamoto, 0000-0002-3648-3572; Ryosuke Takahashi, 0000-0002-1407-9640; Tadashi Isa, 0000-0001-5652-4688.

Submitted Oct 14, 2021. Accepted for publication Feb 05, 2022.
doi: 10.21037/qims-21-969
View this article at: https://dx.doi.org/10.21037/qims-21-969

Introduction

The clinical advantages of 7-Tesla (7T) magnetic resonance imaging (MRI) include high resolution and high contrast for increased lesion detection and applicability to many brain disorders (1-8). However, there are several limitations to using 7T for clinical protocols, such as increased static magnetic field (B0) inhomogeneity, radiofrequency (RF) transmit field (B1+) inhomogeneity, and increased specific absorption rates (SARs), which cause image inhomogeneity. However, applying high-permittivity dielectric pads can mitigate B1+ inhomogeneity (9-11), and signal inhomogeneity correction can be applied to produce highly homogeneous images (12) (*Figure 1*). This review highlights the advantages of 7T neuroimaging for anatomical visualization, presents a brief review of 7T neurochemical measurements and technical issues, and summarizes the principal difficulties of 7T imaging. We recommend other reviews for information on 7T-related safety issues (13-18).

High spatial resolution is achieved at 7T through an increased signal-to-noise ratio (SNR) (19). The tesla ratio of 7/3 is 2.33, and voxels with an isotropic size of 1-mm at 3T have equal SNR to those with an isotropic size of 0.75 mm at 7T, supposing SNR increases linearly to magnetic field strength. However, Pohmann *et al.* reported that SNR increased supra-linearly to the magnetic field strength and that for whole-brain measurements, the SNR at 7T increased by 3.14 relative to the SNR at 3T (20). Thus, a higher SNR can be used to attain higher resolution.

Magnetization-prepared rapid gradient echo (MPRAGE) imaging is a 3-dimensional (3D) T1-weighted imaging (T1WI) and one of the most commonly used sequences, with an isotropic resolution of around 1 mm at 3T. Magnetization-prepared 2 rapid gradient echoes (MP2RAGE) imaging is widely used at 7T (21,22) with an isotropic resolution of around 0.7 mm to provide increased signal and homogeneity (23,24). MP2RAGE combines 2 different images at different inversion times, effectively canceling image inhomogeneity, which is highly advantageous in 7T imaging. Moreover, fitting the longitudinal signal recovery of 2 images provides an additional T1 map (22). This technique has been used to investigate the deep gray matter at 3T (25,26). However, at 7T, higher resolutions have also been used to investigate the cortex (27-29). As an extension, multi-echo MP2RAGE can generate an additional T2* map (30,31) that can be used for multi-contrast segmentation (32), although separate imaging is commonly used.

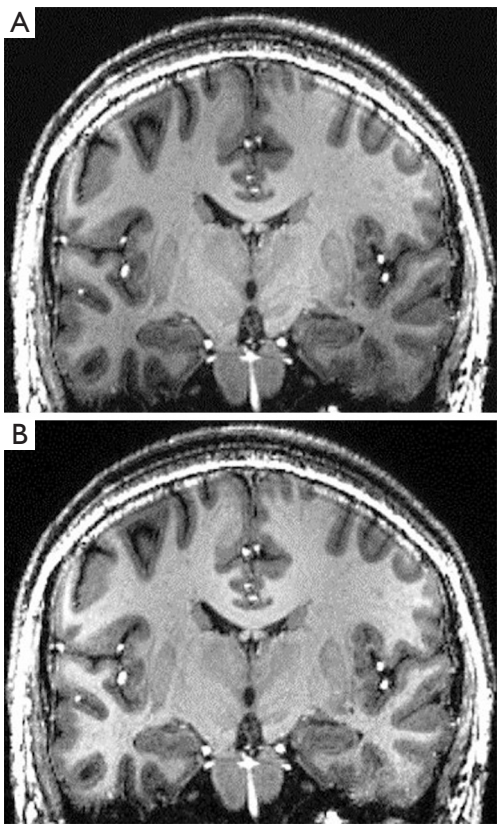

Figure 1 T1-weighted coronal MPRAGE images before (A) and after (B) signal inhomogeneity correction. Gradual signal decrease toward the skull base is corrected. MPRAGE, magnetization-prepared rapid gradient echo.

T2*-weighted imaging (T2*WI) at 7T shows high contrast for myelin and iron. Susceptibility-weighted imaging (SWI) is frequently used at 3T to detect subtle iron depositions (33-37). At 7T, however, high contrast for iron due to the shortening of the T2* value may not require SWI, and T2*WI can also provide anatomical details. High contrast on T2*WI at 7T enabled easier localization of small old hemorrhagic spots within the brain parenchyma than did SWI at 3T (*Figure 2*). However, we found that

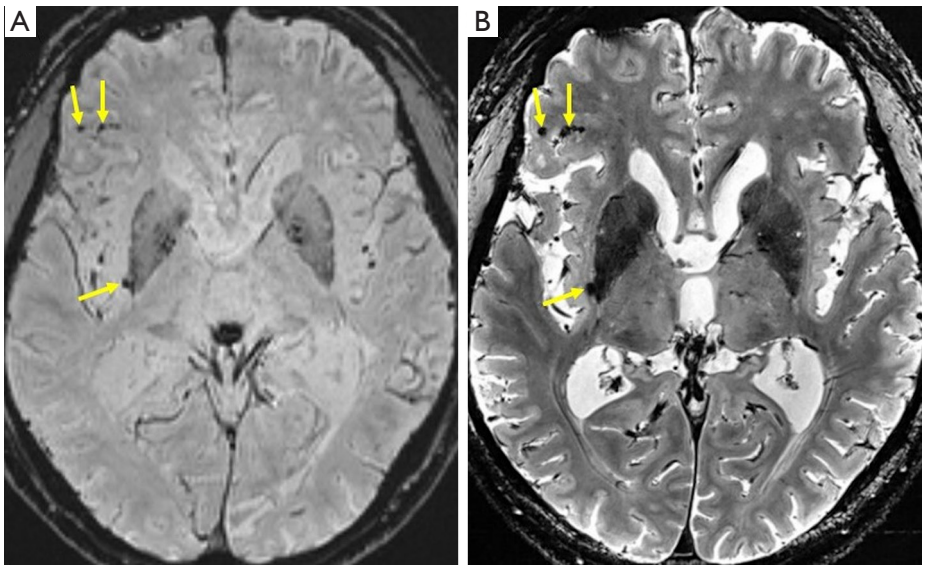

Figure 2 A patient with a traumatic brain injury. (A) SWI at 3T shows small hemorrhagic lesions as low-intensity spots (arrows), but their relation to the background structure is relatively obscured, and their locations in the cortex or sulci are ambiguous. (B) T2*WI at 7T enables easy detection of small hemorrhagic spots (arrows), including their anatomical location. SWI, susceptibility-weighted imaging; T2*WI, T2*-weighted imaging; 3T, 3 Tesla; 7T, 7 Tesla.

7T imaging advantages were brain-region depend, and the advantages of 7T have also been noted in functional MRI (fMRI), where the blood-oxygen level-dependent (BOLD) contrast is reflected on T2*WI (38-40). The degree of chemical shifts of the neural substrates that can be observed using MR spectroscopy (MRS) increases as the static magnetic field increases, enabling high-resolution measurements of the neurochemicals. We present the following article in accordance with the Narrative Review reporting checklist (available at https://qims.amegroups.com/article/view/10.21037/qims-21-969/rc).

Methods of study selection

Although much progress has been made in 7T neuroimaging, the latest image-based findings focusing on regions imaged in relation to pathophysiology need to be clarified. For this review, we analyzed relevant articles found in a search of the PubMed database. The search terms included MR methods, such as "MP2RAGE" and "SWI", and different brain regions. No limitation was set for the year of publication, but if articles were found that covered a similar topic, the most recent one was chosen for our review. Publication status was limited to online or printed studies, and the language of the publication was limited to English. Our primary target was original research articles, although some review articles were included if they contained a brief explanation of 7T neuroimaging that was considered relevant to this review. No explicit exclusion criteria were set, but articles with low relevance to the topics were excluded. When similar studies of clinical investigations were found, those that enrolled a larger number of participants were selected.

A comprehensive description of the results of all the studies we reviewed lies beyond the scope of this paper. However, to illustrate the latest advantages of imaging at 7T, we present a narrative and pictorial review to improve understanding of the current situation and encourage future studies on this topic.

Region-specific advantages of imaging at 7T

The cerebral cortex

The cerebral cortex is one of the main targets of high-resolution imaging, and isotropic 0.7-mm MP2RAGE imaging shows R1 (=1/T1) increase as well as age-related thinning (*Figure 3*). In one study, longitudinal observation of 17 patients over 7 years reported an increase of R1 in the cortex but not in the white matter. The R1 value was shown to highly correlate to the myelin volume fraction in the brain specimen (41). Another study reported that in patients with multiple sclerosis

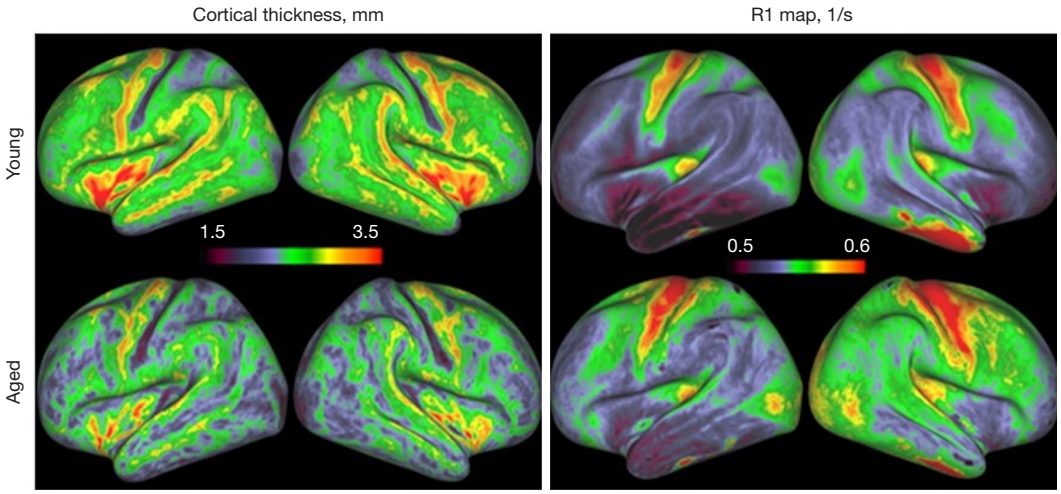

Figure 3 Age-related changes in cortical thickness (mm) and R1 values (1/s) measured using MP2RAGE with 0.7-mm isotropic resolution. Surface maps show the average of 22 young (20–30 years old) and 8 aged (>60 years old) subjects. Decreases in cortical thickness and increases in R1 values are observed by aging. MP2RAGE, magnetization-prepared 2 rapid gradient echoes.

(MS), layer-specific differences were present for cortical R1 and R2* (=1/T2*) values and their negative correlations to the expanded disability status scale (EDSS) was found (42).

In high-resolution T2*WI, magnitude and phase play important roles in cerebral cortex investigations. One of the representative cases was a visualization of the line of Gennari in the primary visual cortex (43) by Fukunaga *et al.*, who observed high densities of both myelin and iron (44). While the R1 and R2* values correlated to the myelin volume fraction and iron concentration, R1 was weighted more on the former and R2* on the latter factor (41). McColgan *et al.* have recently reported high correlations of R2* values across cortical depths to layer-specific cell numbers and layer-specific gene expression (45).

High sensitivity to iron deposition facilitates the detection of tiny hemorrhagic lesions in the cortex and abnormal signals in the white matter (*Figure 4*). One study showed that on T2*WI, a hemorrhagic lesion appeared relatively large due to the blooming effect but appeared much smaller on quantitative susceptibility mapping (QSM) because QSM deconvolves susceptibility dipoles in the phase image for better localization and quantitation of susceptibility. Microinfarcts were found more frequently in patients with intracerebral hemorrhage and suggested a common etiology for underlying small vessel diseases (46), including cerebral amyloid angiopathy (CAA) (47). Cortical microinfarcts have been detected *in vivo* at 7T (48) and found with increased frequency in patients with Alzheimer's disease (AD) (49). Despite their small size, microinfarcts may cause a functional deficit at least 12-fold greater than the volume of the microinfarct core and were shown to contribute to broader brain dysfunction in a mouse model (50). This suggests that microinfarcts are independently associated with cognitive impairment and likely to cause damage to brain structures and function that extends beyond their actual lesion boundaries (51). Other research reported age-related changes observed at 7T as a shortening of cortical T2* values (*Figure 5*) in addition to changes in phase and magnitude (52). Another study found that phase differences between the cortex and the subcortical white matter were larger in early-onset AD than late-onset AD, suggesting the iron load increases in the progress of AD (53). High-resolution SWI at 7T reported senile plaque-like lesions in AD patients *in vivo* (54). These findings are considered to be rooted in the increased *ex vivo* susceptibility observed at 9.4T (55).

Double inversion recovery (DIR) imaging at 3T has been used to detect lesions in the cortex (56,57) and white matter (58,59). High-resolution MPRAGE imaging at 7T has provided complementary information to 3T fluid-attenuated inversion recovery (FLAIR) and DIR for detecting cortical lesions in patients with MS (60). FLAIR and DIR at 7T have performed better than T2*WI (61), but they possess SAR limitations. Pracht *et al.* proposed an optimized 7T 3D DIR scan protocol to decrease SAR and scan time (62). Another option is the use of fluid and white

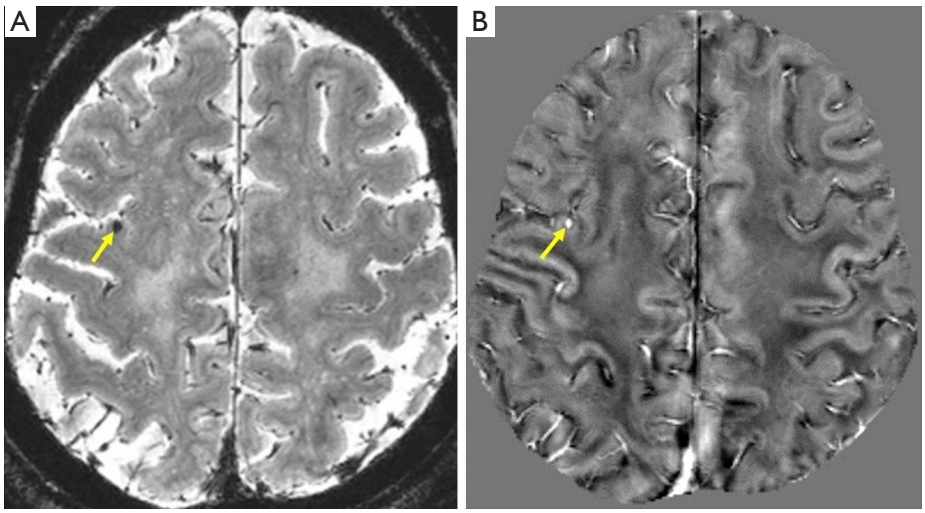

Figure 4 Visualization of a small hemorrhagic lesion. (A) 3D T2*WI shows a small cortical hemorrhage as a low signal intensity spot (arrow). (B) QSM shows a more localized spot (arrow) with high susceptibility by localizing the susceptibility field dipole. 3D, 3-dimensional; QSM, quantitative susceptibility mapping; T2*WI, T2*-weighted imaging.

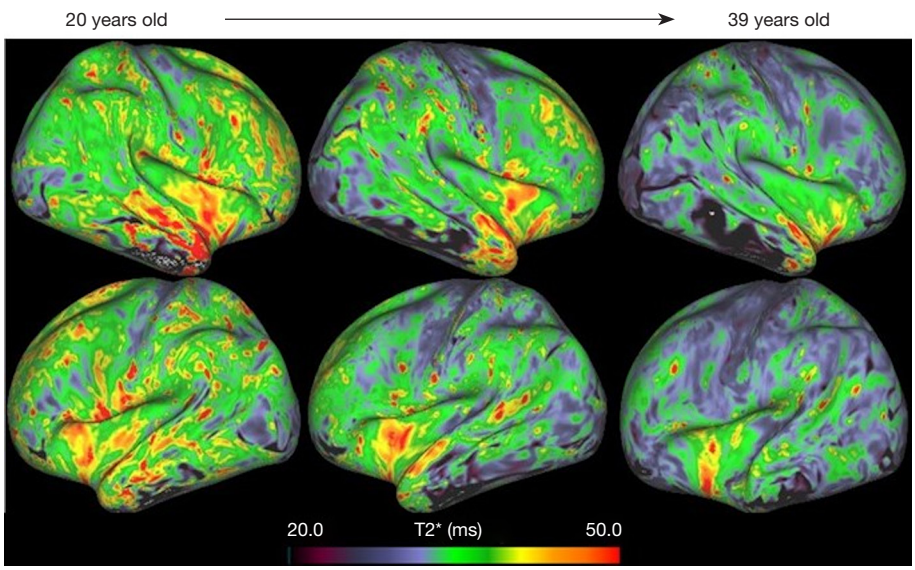

Figure 5 Age-related decreases in cortical T2* values (ms) of healthy participants from 20 to 39 years old. Regional differences are also visualized well.

matter suppression (FLAWS) imaging with an MP2RAGE sequence although the basic contrast is different from DIR (63,64).

Transcortical venules can also be visualized at 7T (*Figure 6*). Blinder *et al.* conducted a histological analysis of the vascular architecture and found that blood flow in penetrating arterioles is effectively drained by the penetrating venules and that lateral perfusion through the vascular network is limited (65). Such vascular architecture is considered to reflect local energy demands. High-resolution BOLD fMRI at 7T has been used to map localized finger-specific sensory activation (66), but its

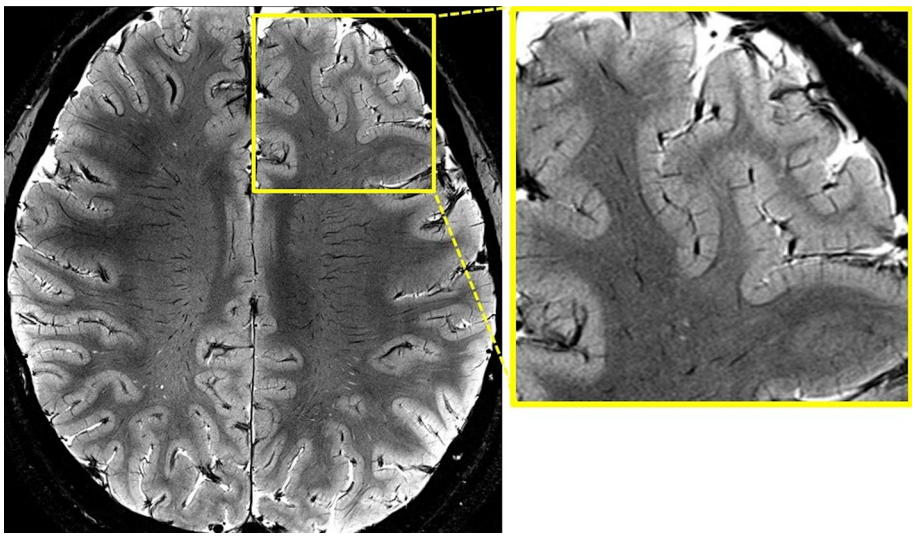

Figure 6 High-resolution 2D T2*WI (0.4 mm × 0.4 mm × 1 mm) shows numerous transcortical venules in addition to the medullary veins and small perivascular spaces. The inset shows an enlarged part of the frontal lobe in greater detail. 2D, 2-dimensional; T2*WI, T2*-weighted imaging.

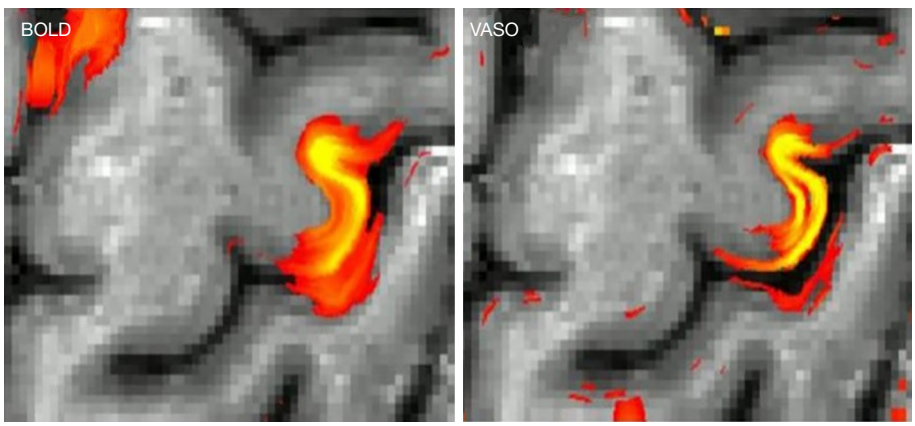

Figure 7 Cortical activation during a right-hand clenching task. BOLD activation is centered at the cortical surface of the left hand-knob area and extends to the postcentral gyrus over the central sulcus. VASO can detect separate activations in the superficial and deep cortical layers of the precentral gyrus and the postcentral gyrus. BOLD, blood-oxygen level-dependent; VASO, vascular space occupancy.

contrast remains dependent on the susceptibility of veins and venules, and the BOLD contrast is not optimal for cortical layer-specific visualization of neural activity. However, data on the vascular architecture can be used to deconvolve the BOLD fMRI signal and reveal cortical layer-specific activity (67,68). Other scan methods, such as vascular space occupancy (VASO) (69-72), have also been used to investigate layer-specific activity by making most of the high SNR of 7T imaging (*Figure* 7) (73-75).

The hippocampus

For subfield evaluation of the hippocampus at 7T, 2D imaging can be conducted with an in-plane resolution of 0.35 mm × 0.35 mm and a slice thickness of 1–2 mm in 5 min. In 3D, a study attained a resolution as high as isotropic 0.35 mm, but the total acquisition time was nearly 15 min (76). Through the use of fMRI with 1.0 mm × 1.0 mm resolution, activation could be localized to subfields of anterior CA2 and CA3 during learning and posterior CA2 and CA1 during retrieval

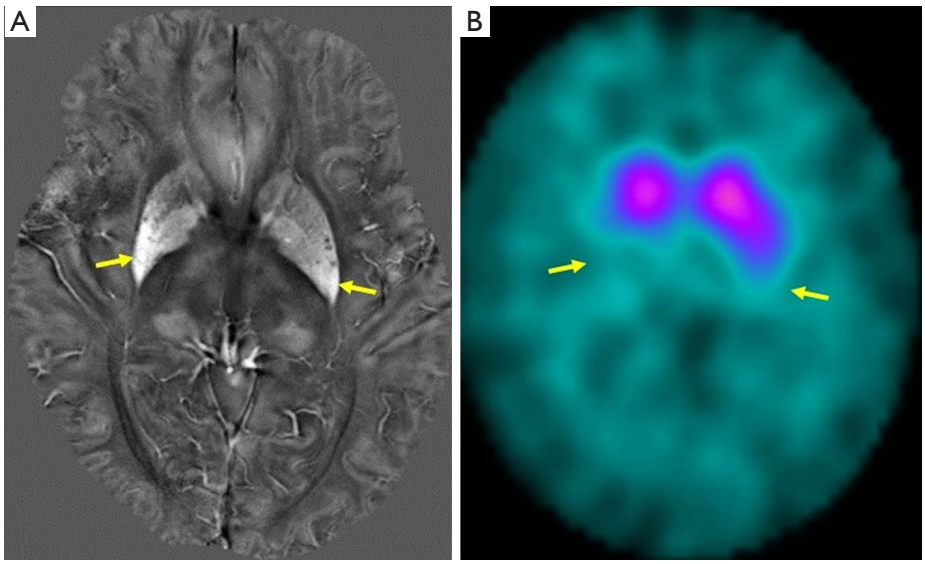

Figure 8 A patient with MSA-P. (A) QSM at 7T shows increased susceptibility at the dorsolateral part of the putamen, particularly on the right side (arrows). (B) Dopamine transporter SPECT imaging shows a reduced specific binding ratio more prominently on the right, indicating a negative correlation between the 2 measurements (arrows). SPECT, single-photon emission computed tomography; QSM, quantitative susceptibility mapping; MSA-P, multiple system atrophy-parkinsonian type; 7T, 7 Tesla.

of novel associations (77).

Pardoe *et al.* conducted automatic segmentation for the hippocampus and amygdala on whole-brain MP2RAGE images with 700-μm isotropic resolution, acquired at 7T using a 3D convolutional neural network (78). The results showed high concordance with those of manual volumetry. Moreover, high-resolution imaging can be exploited to unfold the hippocampus and provide an intrinsic coordinate system for subfield segmentations and quantitative evaluation (79). Recently, after analyzing 21,297 individual brain images, van der Meer *et al.* reported that 6 hippocampal subfield volumes had a significant correlation with 15 unique genome loci (80). The volume of the hippocampal subfields has been related to the decline of memory (81), and specific hippocampal subfields have been more closely associated with memory encoding and retrieval performance in older adults without dementia (82).

The combination of high-resolution 7T imaging and automatic subfield segmentation of the hippocampus has been applied to investigate AD (83), temporal lobe epilepsy (84,85), major depressive disorder (MDD) (86), and vascular risk factors (87). However, caution is required when using MP2RAGE imaging because its T1 reproducibility and volumetry at 7T is affected by B1+ inhomogeneity (88,89).

The deep gray matter

The deep gray matter is a densely populated area of the brain, but only 7% of the individual structures are depicted in standard MRI atlases (90). Many efforts have been made to use 7T imaging for the comprehensive mapping of deep gray structures (91-94). One such effort included the evaluation of 17 prominent subcortical structures using multicontrast imaging (32).

The putamen

This deep nucleus has been investigated in relation to motor-related (95-98) and other neurological disorders. Discriminant analysis using T2* values and mean diffusivity of the putamen at 3T could discriminate among multiple system atrophy-parkinsonian type (MSA-P), Parkinson's disease (PD) (99-101), and healthy control groups (102) with high accuracy. Uchida *et al.* reported a significant negative correlation between susceptibility and dopamine transporter binding ratios at the putamen in patients with PD (103). At 7T, the left-right asymmetry of increased susceptibility at the dorsolateral part of the putamen was similar to the reduction in the specific binding ratio of the dopamine-transporter single-photon emission computed tomography (SPECT) imaging (*Figure 8*). Patients with premanifest Huntington's disease had significantly higher

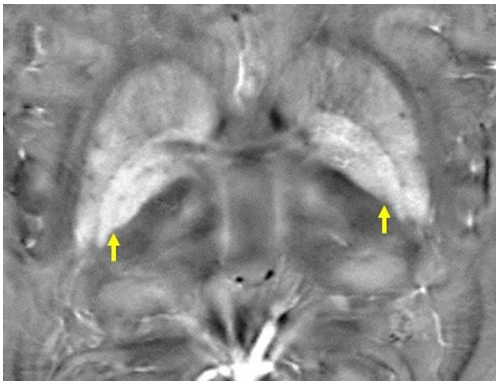

Figure 9 An axial QSM image of a healthy subject at the basal ganglia. The globus pallidus interna is separated from the externa by the medial medullary lamina (arrows), which is visualized as a thin layer of low signal intensity. Differences in susceptibility can also be observed among the thalamic subnuclei. QSM, quantitative susceptibility mapping.

susceptibility values in the caudate nucleus and putamen, where the values were inversely correlated with structure volumes (104). In fMRI, the putamen and globus pallidus suffer from substantial signal loss due to their high susceptibility, and conventional single-echo echo-planar imaging (EPI) for functional imaging is subject to a lower temporal SNR (tSNR) than it is for cortical imaging. Multiecho EPI can increase tSNR by 84%, on average (105).

The globus pallidus

Separation of the globus pallidus interna (GPi) and externa (GPe) is important for deep brain stimulation (DBS) (106,107) when the GPi is the target for DBS and accurate electrode localization inside the GPi is required for successful treatment. The GPi is separated from the GPe by the medial medullary lamina (MML) and further subdivided into external and internal segments (GPie/GPii, respectively) by the accessory medullary lamina (AML) (108,109). Separation of the globus pallidus into substructures is expected to reveal pathological changes. Maruyama *et al.* (110) successfully visualized the internal structures of the GPi segments at 7T (*Figure 9*), and the substructures have been segmented automatically using deep-learning with 7T data (111). In another study, higher globus pallidus and red nucleus susceptibility was found more often in a progressive supranuclear palsy (PSP) group than in PD, MSA, and healthy control groups (102). The globus pallidus is also related to schizophrenia. In an analysis of 778 patients, Hashimoto *et al.* found that illness duration was positively associated with bilateral globus pallidus volumes (112). Direct and indirect pathways from the cortex have overlapping projections to the GPe, and it has been suggested that the 2 pathways work cooperatively via interactions within the GPe (113).

The thalamus

The thalamus consists of many subnuclei connected to different areas of the cortex and spinal cord and is associated with behavioral (114) and cognitive changes related to many neurological disorders, including MS (115-117) and PD (94,118), among others. The subnuclei have different relaxation properties and orientation alignments that are dependent on their projections. This knowledge enables segmentation of the thalamic subnuclei (119-124). Quantitative measurement of T1 and T2 values at 3T can also segment the thalamic subnuclei mapped on the T1/T2 feature-space, but the scan time can be lengthy (125). At 7T, Tourdias *et al.* optimized MPRAGE imaging and delineated deep gray matter structures, including the thalamic subnuclei, by nullifying the white matter with sufficient SNR (126). Automatic segmentation has also been conducted using MP2RAGE (127), SWI (128), or multicontrast images (119,129). Analysis at the level of the subnuclei is expected to help in the investigation of various sorts of neurological disorders.

The habenula

Located medial to the thalamus, the habenula is a tiny but highly important functional structure. It is involved in behavioral responses to pain, stress, anxiety, sleep, and reward, and its dysfunction is associated with depression, schizophrenia, and drug-induced psychosis (130). An increased habenula volume has been observed with 0.7-mm isotropic resolution MP2RAGE imaging at 7T in patients with unmedicated MDD (131). At 7T, resolutions as high as isotropic 0.5 mm can be reached, and details of the habenula can be visualized (*Figure 10*). High-resolution imaging is extremely useful in observing the habenula, which is divided into functionally distinct medial and lateral nuclei that have different influences on the subcortical reward and mood systems (132). The medial section modulates the activity of the interpeduncular nucleus and influences monoamine signaling (133),

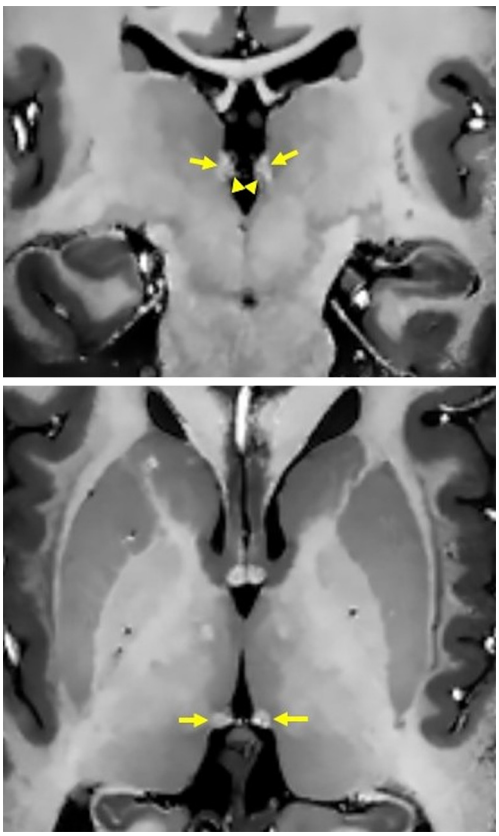

Figure 10 High-resolution T1WI (0.5 mm isotropic resolution) of the habenula (arrows) acquired using MP2RAGE after denoising (top: coronal, bottom: axial). On the coronal image, the lateral nucleus shows a slightly higher signal reflecting a shorter T1 value than that of the medial nucleus (arrowheads). T1WI, T1-weighted imaging; MP2RAGE, magnetization-prepared 2 rapid gradient echoes.

whereas the lateral part mediates the inhibition of the ventral tegmental area and downregulates mesolimbic reward activity (134,135). The lateral nucleus has shorter T1 and T2* values than does the medial nucleus (136). High-resolution T1-weighted over T2*-weighted images at 7T has been shown to enable habenula segmentation (137). It should also be noted that high-resolution functional MRI at 7T is capable of visualizing the connectivity of small structures such as the habenula (*Figure 11*).

The brain stem

Observation of the brain stem also benefits from imaging at 7T, which permits the visualization of small structures, such as the subthalamic nucleus (STN) separate from the substantia nigra (SN). The nigrosome-1 located at dorsolateral part of the SN can also be clearly depicted.

The STN

The STN is located in close proximity to the SN. Separation of these structures *in vivo* has been difficult, but 7T imaging can clearly distinguish between them (*Figure 12*). Like the GPi, the STN is targeted in DBS to treat movement disorders (138-140). Higher iron concentrations have been reported within the STN at the medial-inferior area (141), and age-related changes have been found in the medial-to-lateral directions on 7T images (142). In a streptozotocin-treated animal model of sporadic AD, QSM found largely decreased susceptibility in the STN in the AD model compared to healthy controls, suggesting that this alteration may reflect neuronal death and serve as a biomarker in AD (143). The STN and SN are functionally segregated, but fMRI studies have not been able to fully separate their signals (144). De Hollander *et al.* demonstrated that fMRI at 7T with the appropriate parameters could better detect the activation of the STN and other deep gray matter nuclei (145).

The SN

The SN pars compacta (SNpc) accommodates many dopaminergic neurons and contains neuromelanin (NM) and high amount of iron. Iron and NM play an important role in controlling multiple brain functions, including voluntary movement and behavioral processes. NM-sensitive and iron-sensitive images have been used to analyze the SN (5,146). Heavily T1WI is sensitive to the paramagnetic properties of NM and shows NM-containing area as having high signal intensity (147-151). Reduced SNpc size and contrast ratio have been reported in patients with PD when they were compared with healthy control subjects using NM-sensitive imaging with high differential capability (152). NM imaging has predominantly been conducted at 3T due to limitations in SARs.

The susceptibility of SNpc was increased in patients with PD relative to healthy control subjects (102). According to several studies, nigrosome-1, a densely aggregated area of dopaminergic neurons inside the SNpc, is better visualized using iron-sensitive imaging, such as T2*WI, SWI, and QSM (94,138,153-155). It displays as a

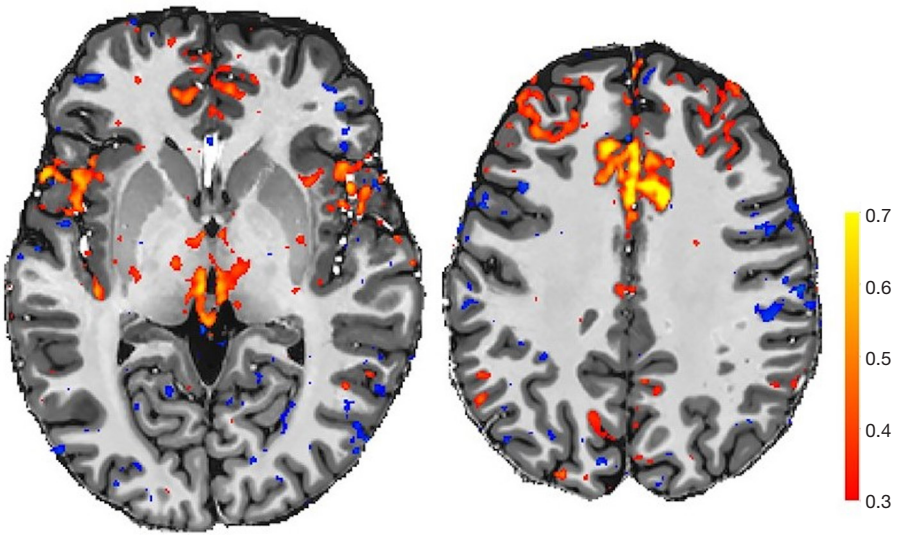

Figure 11 Connectivity between the habenula (seed) and other brain regions, including the anterior cingulate cortex, can be detected using high-resolution functional MRI (1.6 mm isotropic resolution). The color bar shows the correlation coefficients of the time-course signal. MRI, magnetic resonance imaging.

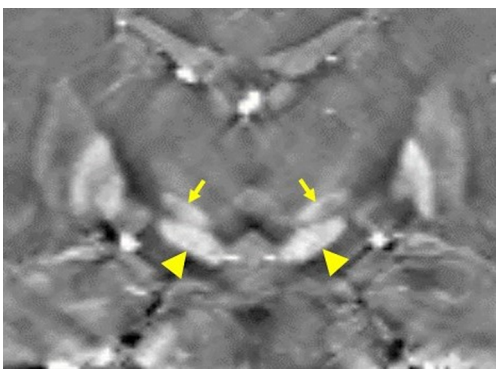

Figure 12 A coronal QSM image of the midbrain (0.5 mm isotropic resolution). The subthalamic nucleus (arrows) can be easily separated from the substantia nigra (arrowheads). QSM, quantitative susceptibility mapping.

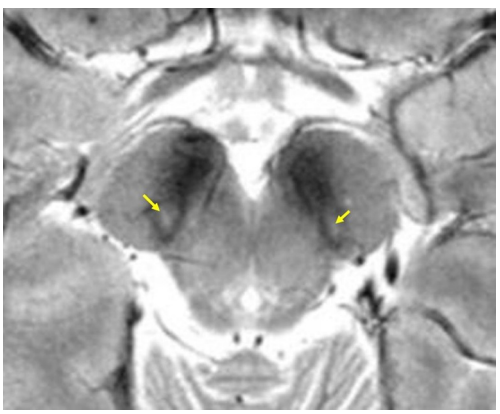

Figure 13 T2*WI at 7T (0.4 mm × 0.4 mm × 1 mm) enables clear visualization of the nigrosome-1 (arrows) in a healthy subject. T2*WI, T2*-weighted imaging.

hyperintense, ovoid area at the dorsolateral border of the otherwise hypointense SNpc in healthy control subjects. This imaging feature has been named the "swallow-tail sign" (156). Loss of this sign is recognized as a diagnostic imaging biomarker of PD (157-161). Imaging at 7T is excellent for evaluating nigrosome-1 (*Figure 13*) and has been used to diagnose PD, MSA, and PSP (146,162,163). However, aging decrements this hyperintensity (164) and its loss is often a common factor in these disorders, making it difficult to discriminate them (165).

The cerebral white matter

Many structural and connectivity studies have been conducted using diffusion tensor imaging (DTI) (166-168) for various types of disorders, such as AD (169-172), PD (173-175), schizophrenia (176), MDD (177,178), bipolar disorder (179), and traumatic brain injury (TBI) (180,181). The SNR of DTI increases supralinearly to the increase in magnetic field strength, partly due to improved hardware (182). This trait can be used to investigate neurological

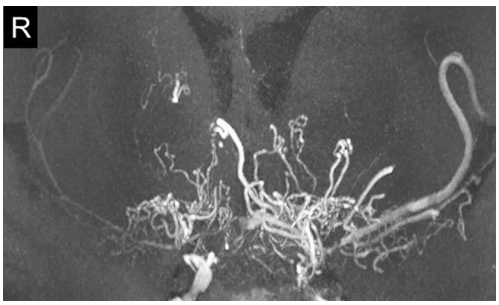

Figure 14 Coronal maximum intensity projection MR angiography of a patient with Moyamoya disease. The 0.25-mm isotropic resolution was acquired in 6 min. Dilated lenticulostriate arteries for collateral circulation are fewer on the right side (indicated as R), and the distal part of the middle cerebral artery is hypovisualized on the same side. MR, magnetic resonance.

disorders. The semiautomatic segmentation of 72 major white-matter tracts was technically feasible (183). This method was developed using 3T DTI data from the human connectome project (HCP) and validated using other 3T DTI data with various scan parameters. This method is expected to be applicable to high-resolution 7T DTI data.

Cerebral microbleeds (CMBs) are small chronic brain hemorrhages that are likely to be caused by abnormalities in the small vessels of the brain. One study revealed that in 72% of patients with moderate-to-severe head injury, diffuse axonal injury was found in the form of traumatic CMBs (184). In another study, the total number of traumatic CMBs in 10 patients were 485 and 584 using SWI at 3T and 7T, respectively with a similar spatial resolution. The number of observed lesions increased to 684 at 7T when a higher spatial resolution was used (185). Radiation therapy is associated with CMBs in brain tumors (186). Observation at 7T found the total number and volume of CMBs increased annually by 18% and 11%, respectively, while fractional anisotropy (FA) decreased by a median of 6.5% per year (187). CMBs have shown an increasing association with AD in imaging conducted at a higher magnetic field (188). Deposition of β-amyloid on PET imaging was increased at CMB sites (189-191).

The perivascular space (PVS)

Dilated PVSs at the level of the centrum semiovale are a marker of underlying arteriopathy in patients with lobar hemorrhage (192) and are highly prevalent in sporadic CAA and superficial siderosis, which impair interstitial fluid drainage from the cerebral white matter (193). CMBs are an indirect marker of CAA, and MRI-visible PVS is considered to be related to this pathology. The dilatation of the juxtacortical PVS was significantly higher around CMBs than at the reference sites, and this colocalization suggests common underlying pathophysiology that is most likely to be CAA (194). The PVSs are more clearly displayed when a higher resolution is employed (195). High-resolution 3D T2-weighted brain imaging at 7T has enabled the automatic segmentation of small, hyperintense, fluid-filled PVSs and shown a significant increase in PVS density in patients with AD (196).

Recent MR investigations suggest that PVS is related to the glymphatic system (197-204), a waste-draining system within the brain (205-208). Naganawa *et al.* suggested that the space between the pial sheath and the cortical venous wall may connect to the meningeal lymphatics. Their study used a gadolinium-based contrast agent and 3D-real inversion recovery imaging at 3T (209). Taoka *et al.* detected a reduction in glymphatic activity along the PVS using DTI in patients with AD (210). High-resolution 7T imaging could depict PVS along small arterial branches, including the lenticulostriate arteries (LSA) (211).

The cerebral vasculature

The T1 value is longer at 7T than at 3T, which is highly advantageous to visualizing distal small branches by suppressing the background signal in MR angiography (MRA). In addition to stroke, moyamoya disease (MMD) is one of the most common vascular stenosis disorders, especially in Asia. In MMD, stenosis is observed at the circle of Willis, and collateral circulation has been evaluated using contrast-enhanced CT angiography (212) and black-blood MRA at 1.5T and 3T (213-215). However, at 7T, conventional inflow MRA can visualize the LSA as bright blood at a resolution of approximately 0.25 mm, assisting in the investigation of pathological conditions (216-223). One case we reviewed (*Figure 14*) showed a patient with MMD and dilated LSA branches for collateral circulation. In the same patient, the FLAIR "ivy sign", showing the slow retrograde flow of dilated pial vasculature (224), was depicted more clearly at 7T than at 3T. Increased susceptibility at the ischemic lesions and medullary veins (225) was also observed in the right frontal area (*Figure 15*). Uwano *et al.* were able to detect impaired cerebrovascular reactivity in patients with chronic cerebral ischemia using whole-brain 7T MRA (226).

Arterial spin labeling (ASL) has been used to visualize

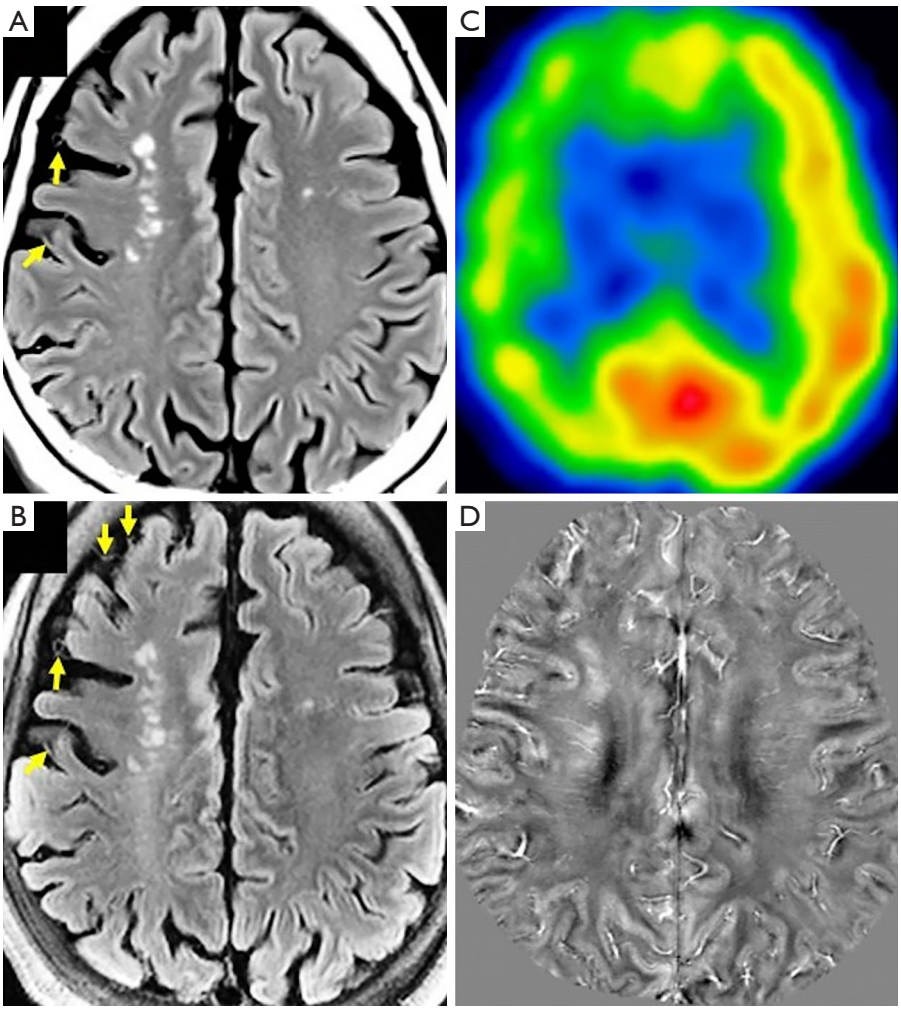

Figure 15 The same patient as in *Figure 12*. FLAIR images acquired at 3T (A) and 7T (B). Both images show similar white-matter lesions as hyperintense, but "ivy-signs", representing slow collateral flow, are better depicted at 7T (arrows). (C) CBF measured using iodine-123 N-isopropyl-p-iodoamphetamine SPECT at rest. CBF is widely lower on the right frontal area. (D) QSM acquired at 7T (0.5 mm isotropic resolution) shows increased susceptibility at the cortex, medullary veins, and ischemic lesions in the same area. The right side of the images shows the left side of the patient. CBF, cerebral blood flow; FLAIR, fluid-attenuated inversion recovery; 3T, 3 Tesla; 7T, 7 Tesla; SPECT, single-photon emission computed tomography; QSM, quantitative susceptibility mapping.

cerebral blood flow (CBF). Togao *et al.* showed distal circulation in MMD and arterio-venous malformation using 4D-ASL at 3T (227-229). ASL at 7T benefits from T1 prolongation for measuring CBF when appropriate spin labeling methods are implemented (230-234). Kashyap *et al.* applied ASL at submillimetric resolutions to observe cortical laminar fMRI responses (233). In addition to blood flow, vascular wall imaging, such as delay alternating with nutation for tailored excitation (DANTE) prepared imaging, has been optimized for 7T (235) and can be used to check vascular wall lesions.

MRS and chemical exchange saturation transfer (CEST) imaging

Chemical shift increases in correlation to increase in magnetic field strength. MRS at 7T better separates neurochemicals and increases detectability compared with measurements at lower magnetic fields (236). Due to 7T's higher SNR (237), a small amount of averaging is able to attain sufficient SNR, and scan time can be reduced (238). High measurement repeatability is also attained at 7T (239-245). MRS at 7T has been used to investigate multiple

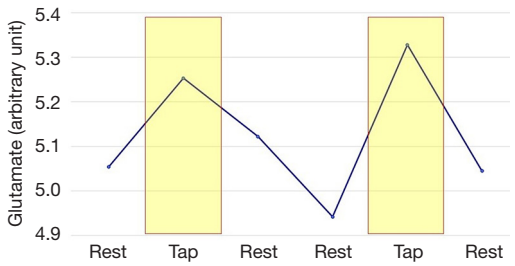

Figure 16 Dynamic glutamate changes during conditions of rest and the right finger tapping (each for 2.5 min) observed in the left motor cortex using 7T. Glutamate increases were observed during tapping (yellow boxes). 7T, 7 Tesla.

brain regions or specific neurochemicals in many disorders, such as brain tumors (246), epilepsy (247), MS (248), schizophrenia/psychosis (249-252), depression (253,254), attention-deficit hyperactive disorder (ADHD) (255), among others. It has also been used to observe dynamic changes in neurotransmitters (*Figure 16*) (256,257).

MRS imaging (MRSI) is frequently used for 2D and 3D investigation. In MRSI, 2D ultra-short TE imaging at 9.4T has enabled measurements of low-concentration neurochemicals, such as gamma-aminobutyric acid (GABA), glutamine, aspartate, and taurine (258). In addition, this 2D scan was successfully accelerated to 5.6 times faster, applying deep-learning for high-resolution metabolite maps (matrix size of 64×64) in 2.8 min (259). At 7T, high-resolution MRSI with a matrix size of 100×100 clearly displayed the neurochemical profiles of MS plaques (260) and glial tumors, including the edematous or infiltrated surroundings (261). MRSI measurement has enabled area-wise correlation mapping between many pairs of neurochemical concentrations and elucidated differences between patients with epilepsy and healthy control subjects (262). In addition to neurochemicals, macromolecules (MMs) are drawing growing attention. They confound the quantitation of neurochemicals, and spectral editing (263) has been used to investigate metabolites, such as GABA, in small quantities (264). However, MMs are physiological metabolites, and their quantities may indicate pathological states (265,266).

CEST imaging can also be used to obtain 2D/3D information of a specific metabolite. It saturates mobile protons in amide (-NH), amine ($-NH_2$), and hydroxyl (-OH), among others, and these protons are exchanged with those of the bulk water (267-270). One of the representative applications is amide proton transfer (APT)-weighted imaging that suppresses the signal of amide protons located 3.5 ppm away from the water signal (271). APT imaging has been widely used at 3T to investigate brain tumors (272-277). At 7T, additional CEST measurements are conducted for such effects as the nuclear Overhauser effect (NOE) (278,279), among others (280). Glutamate is another important target for brain CEST imaging at 7T. Glutamate-specific CEST is known as GluCEST (281). Higher concentrations of glutamate were found on the epileptogenic side in patients of nonlesional temporal lobe epilepsy (282,283). GluCEST showed low concentrations in patients on the psychosis spectrum (284).

Technical issues

Our review found that not all studies were able to visualize all brain areas well at 7T. Signal reduction or dropout and image distortion were frequently observed in regions at the skull base, such as the orbitofrontal and inferior temporal areas. Signal reduction was also observed in the cerebellum. There are several major technical problems related to these phenomena: B0 inhomogeneity, B1+ inhomogeneity (20) and increased SAR (285). Local B0 inhomogeneity results in signal defects, and information on some parts of the brain, especially at the skull base, remains unobtainable. It also introduces structural distortion, and corrections are thus crucial for surface-based analysis at 7T (286). Moreover, B0 fluctuation caused by respiration can deteriorate image quality. It can be monitored using field probes (287), and real-time correction improved the quality of T2*WI (288), high-resolution MRA (289), and QSM imaging (290,291). With motion correction, the whole brain could be scanned at a 380-μm isotropic resolution, taking nearly 1 hour (292), although real-time B0 correction and sequences that can cope with such correction are not readily available for implementation. We consider the use of simultaneous multislice (SMS) 2D gradient echo imaging might be an alternative. Its SNR was lower than that of 3D imaging by 13.0% to 17.6%, but SMS 2D susceptibility imaging was found to generate significantly higher gray/white matter or globus pallidus/putamen contrast by 13.3% to 87.5% (293) due to a much longer time of repetition (TR). SMS 2D imaging is more robust because the motion artifact affects only a single slice or several slices, and it is considered suitable for patients who cannot keep still for a long time.

To improve B1+ inhomogeneity, high permittivity dielectric pads are frequently placed at the bilateral zygomatic areas and/or the back of the head (9,294), but

Figure 17 Images at 50-µm isotropic resolution of a mouse brain *ex vivo* in coronal (A) and axial (B) orientations acquired using an unwired small-sized volume coil inserted into a knee coil.

they are not perfect. At low B1+ areas, such as the skull base, the gray-to-white contrast is reduced, resulting in segmentation errors (295). When compared to 3T in voxel-based morphometry, higher gray-matter volumes have been estimated for 7T, predominantly in the superior cortical areas, the caudate nucleus, cingulate cortex, and hippocampus, whereas the opposite has been found in the inferior cortical areas of the cerebrum, putamen, thalamus, and cerebellum (296). Misclassifications have been observed in the lower brain areas, and caution should be paid to these areas. This error can be mitigated by correcting the B1+ inhomogeneity (88) using the transmit field map (297).

Parallel transmission (pTx) has been shown to increase B1+ uniformity across the brain (298). In resting-state fMRI at 7T, RF shimming (299) reduced the coefficient of variation for whole-brain flip-angle distribution by nearly 40% on average (300) and increased the signal uniformity of 3D T2-weighted imaging (301). Such pTx with RF shimming is advantageous at 7T, but it takes a long time and is accompanied by a certain risk of local SAR increases, known as "hot spots" (302). A simpler option is the *k-t* point pulse (303,304). This has recently been implemented as the universal pulse (UP) and allows "plug and play" use without subject-specific measurement and optimization (305), while maintaining low intersubject variability for safety (306). The UP has achieved flip-angle homogeneity comparable to that of a clinical 3T system (307). It was used for 3D T2WI with higher signal homogeneity at 7T (308,309). Recent advances in machine learning have opened the way for a different approach to calibration-free dynamic RF shimming (310).

MR findings need to be validated by histopathology, animal models, autopsy specimens, and other lines of evidence. MR imaging with higher resolutions can be conducted using the 7T human MR system but requires an additional transmit-receive coil system. A small-size volume coil that can be inserted into a vendor-provided coil without wiring offers easy implementation. Okada *et al.* recently fabricated such coils and presented high-resolution images of small specimens (*Figure 17*) (311). Implementation in this manner is expected to extend the role of 7T imaging.

Conclusions

This review examined the advantages of increased contrast, resolution, and specificity in visualizing the pathophysiological conditions of many neurological disorders. We found that neuroimaging at 7T has helped to identify neurodegenerative changes and potential biomarkers that are not visible under lower magnetic field strengths. However, many study reports were limited by small-size participant cohorts and/or the absence of longitudinal data (312). To overcome these limitations, many collaborative investigations, such as the European ultra-high field imaging network for neurodegenerative diseases (EUFIND) (313), are encouraging the use of 7T neuroimaging in clinical and research applications. The 7T human MR system is expected to be an indispensable tool in the near future.

Acknowledgments

Funding: This work was supported by The Strategic

International Brain Science Research Promotion Program (Brain/MINDS Beyond; 21dm0307003h0004 and 21dm0307102h0003) from the Japanese Agency for Medical Research and Development (AMED), the Japan Society for the Promotion of Science (JSPS) KAKENHI grants-in-aid for scientific research B (21H03806), and Siemens Healthcare KK, Japan.

Footnote

Reporting Checklist: The authors have completed the Narrative Review reporting checklist. Available at https://qims.amegroups.com/article/view/10.21037/qims-21-969/rc

Conflicts of Interest: All authors have completed the ICMJE uniform disclosure form (available at https://qims.amegroups.com/article/view/10.21037/qims-21-969/coif). TO receives a research grant from Siemens Healthcare K.K., Japan and the JSPS (21H03806). TO serves as an unpaid editorial board member for *Quantitative Imaging in Medicine and Surgery*. NS and TM receive grants from AMED (21dm0307003h0004 and 21dm0307102h0003, respectively). The other authors have no conflicts of interest to declare.

Ethical Statement: The authors are accountable for all aspects of the work in ensuring that questions related to the accuracy or integrity of any part of the work are appropriately investigated and resolved. The 7T human MR system has not been approved for clinical use in Japan. Imaging at 7T was conducted under the approval of the local institutional review board (Y1143).

References

1. Balchandani P, Naidich TP. Ultra-High-Field MR Neuroimaging. AJNR Am J Neuroradiol 2015;36:1204-15.
2. Düzel E, Costagli M, Donatelli G, Speck O, Cosottini M. Studying Alzheimer disease, Parkinson disease, and amyotrophic lateral sclerosis with 7-T magnetic resonance. Eur Radiol Exp 2021;5:36.
3. Shlobin NA, Singh G, Newton CR, Sander JW. Classifying epilepsy pragmatically: Past, present, and future. J Neurol Sci 2021;427:117515.
4. Wei RL, Wei XT. Advanced Diagnosis of Glioma by Using Emerging Magnetic Resonance Sequences. Front Oncol 2021;11:694498.
5. Bae YJ, Kim JM, Sohn CH, Choi JH, Choi BS, Song YS, Nam Y, Cho SJ, Jeon B, Kim JH. Imaging the Substantia Nigra in Parkinson Disease and Other Parkinsonian Syndromes. Radiology 2021;300:260-78.
6. Rondinoni C, Magnun C, Vallota da Silva A, Heinsen HM, Amaro E Jr. Epilepsy under the scope of ultra-high field MRI. Epilepsy Behav 2021;121:106366.
7. Cope TE, Weil RS, Düzel E, Dickerson BC, Rowe JB. Advances in neuroimaging to support translational medicine in dementia. J Neurol Neurosurg Psychiatry 2021;92:263-70.
8. Opheim G, van der Kolk A, Markenroth Bloch K, Colon AJ, Davis KA, Henry TR, et al. 7T Epilepsy Task Force Consensus Recommendations on the Use of 7T MRI in Clinical Practice. Neurology 2021;96:327-41.
9. Teeuwisse WM, Brink WM, Webb AG. Quantitative assessment of the effects of high-permittivity pads in 7 Tesla MRI of the brain. Magn Reson Med 2012;67:1285-93.
10. Vaidya MV, Sodickson DK, Collins CM, Lattanzi R. Disentangling the effects of high permittivity materials on signal optimization and sample noise reduction via ideal current patterns. Magn Reson Med 2019;81:2746-58.
11. van Gemert J, Brink W, Webb A, Remis R. High-permittivity pad design tool for 7T neuroimaging and 3T body imaging. Magn Reson Med 2019;81:3370-8.
12. Uwano I, Kudo K, Yamashita F, Goodwin J, Higuchi S, Ito K, Harada T, Ogawa A, Sasaki M. Intensity inhomogeneity correction for magnetic resonance imaging of human brain at 7T. Med Phys 2014;41:022302.
13. Okada T, Akasaka T, Thuy DH, Isa T. Safety for Human MR Scanners at 7T. Magn Reson Med Sci 2021. [Epub ahead of print]. doi: 10.2463/mrms.rev.2021-0063.
14. Fagan AJ, Bitz AK, Björkman-Burtscher IM, Collins CM, Kimbrell V, Raaijmakers AJE; ISMRM Safety Committee. 7T MR Safety. J Magn Reson Imaging 2021;53:333-46.
15. Hansson B, Markenroth Bloch K, Owman T, Nilsson M, Lätt J, Olsrud J, Björkman-Burtscher IM. Subjectively Reported Effects Experienced in an Actively Shielded 7T MRI: A Large-Scale Study. J Magn Reson Imaging

2020;52:1265-76.
16. Hoff MN, McKinney A 4th, Shellock FG, Rassner U, Gilk T, Watson RE Jr, Greenberg TD, Froelich J, Kanal E. Safety Considerations of 7-T MRI in Clinical Practice. Radiology 2019;292:509-18.
17. Kraff O, Quick HH. 7T: Physics, safety, and potential clinical applications. J Magn Reson Imaging 2017;46:1573-89.
18. Uwano I, Metoki T, Sendai F, Yoshida R, Kudo K, Yamashita F, Higuchi S, Ito K, Harada T, Goodwin J, Ogawa A, Sasaki M. Assessment of sensations experienced by subjects during MR imaging examination at 7T. Magn Reson Med Sci 2015;14:35-41.
19. Springer E, Dymerska B, Cardoso PL, Robinson SD, Weisstanner C, Wiest R, Schmitt B, Trattnig S. Comparison of Routine Brain Imaging at 3 T and 7 T. Invest Radiol 2016;51:469-82.
20. Pohmann R, Speck O, Scheffler K. Signal-to-noise ratio and MR tissue parameters in human brain imaging at 3, 7, and 9.4 tesla using current receive coil arrays. Magn Reson Med 2016;75:801-9.
21. Marques JP, Kober T, Krueger G, van der Zwaag W, Van de Moortele PF, Gruetter R. MP2RAGE, a self bias-field corrected sequence for improved segmentation and T1-mapping at high field. Neuroimage 2010;49:1271-81.
22. Marques JP, Gruetter R. New developments and applications of the MP2RAGE sequence--focusing the contrast and high spatial resolution R1 mapping. PLoS One 2013;8:e69294.
23. O'Brien KR, Kober T, Hagmann P, Maeder P, Marques J, Lazeyras F, Krueger G, Roche A. Robust T1-weighted structural brain imaging and morphometry at 7T using MP2RAGE. PLoS One 2014;9:e99676.
24. O'Brien KR, Magill AW, Delacoste J, Marques JP, Kober T, Fautz HP, Lazeyras F, Krueger G. Dielectric pads and low- B1+ adiabatic pulses: complementary techniques to optimize structural T1 w whole-brain MP2RAGE scans at 7 tesla. J Magn Reson Imaging 2014;40:804-12.
25. Okubo G, Okada T, Yamamoto A, Kanagaki M, Fushimi Y, Okada T, Murata K, Togashi K. MP2RAGE for deep gray matter measurement of the brain: A comparative study with MPRAGE. J Magn Reson Imaging 2016;43:55-62.
26. Okubo G, Okada T, Yamamoto A, Fushimi Y, Okada T, Murata K, Togashi K. Relationship between aging and T1 relaxation time in deep gray matter: A voxel-based analysis. J Magn Reson Imaging 2017;46:724-31.
27. Marques JP, Khabipova D, Gruetter R. Studying cyto and myeloarchitecture of the human cortex at ultra-high field with quantitative imaging: R1, R2* and magnetic susceptibility. Neuroimage 2017;147:152-63.
28. van der Zwaag W, Buur PF, Fracasso A, van Doesum T, Uludağ K, Versluis MJ, Marques JP. Distortion-matched T1 maps and unbiased T1-weighted images as anatomical reference for high-resolution fMRI. Neuroimage 2018;176:41-55.
29. Fujimoto K, Polimeni JR, van der Kouwe AJ, Reuter M, Kober T, Benner T, Fischl B, Wald LL. Quantitative comparison of cortical surface reconstructions from MP2RAGE and multi-echo MPRAGE data at 3 and 7 T. Neuroimage 2014;90:60-73.
30. Metere R, Kober T, Möller HE, Schäfer A. Simultaneous Quantitative MRI Mapping of T1, T2* and Magnetic Susceptibility with Multi-Echo MP2RAGE. PLoS One 2017;12:e0169265.
31. Alkemade A, Mulder MJ, Groot JM, Isaacs BR, van Berendonk N, Lute N, Isherwood SJ, Bazin PL, Forstmann BU. The Amsterdam Ultra-high field adult lifespan database (AHEAD): A freely available multimodal 7 Tesla submillimeter magnetic resonance imaging database. Neuroimage 2020;221:117200.
32. Bazin PL, Alkemade A, Mulder MJ, Henry AG, Forstmann BU. Multi-contrast anatomical subcortical structures parcellation. Elife 2020;9:59430.
33. Mori N, Miki Y, Kikuta K, Fushimi Y, Okada T, Urayama S, Sawamoto N, Fukuyama H, Hashimoto N, Togashi K. Microbleeds in moyamoya disease: susceptibility-weighted imaging versus T2*-weighted imaging at 3 Tesla. Invest Radiol 2008;43:574-9.
34. Haacke EM, Xu Y, Cheng YC, Reichenbach JR. Susceptibility weighted imaging (SWI). Magn Reson Med 2004;52:612-8.
35. Haacke EM, Mittal S, Wu Z, Neelavalli J, Cheng YC. Susceptibility-weighted imaging: technical aspects and clinical applications, part 1. AJNR Am J Neuroradiol 2009;30:19-30.
36. Tong KA, Ashwal S, Holshouser BA, Shutter LA, Herigault G, Haacke EM, Kido DK. Hemorrhagic shearing lesions in children and adolescents with posttraumatic diffuse axonal injury: improved detection and initial results. Radiology 2003;227:332-9.
37. Wycliffe ND, Choe J, Holshouser B, Oyoyo UE, Haacke EM, Kido DK. Reliability in detection of hemorrhage in acute stroke by a new three-dimensional gradient recalled echo susceptibility-weighted imaging technique compared to computed tomography: a retrospective study. J Magn Reson Imaging 2004;20:372-7.

38. Ogawa S, Lee TM, Kay AR, Tank DW. Brain magnetic resonance imaging with contrast dependent on blood oxygenation. Proc Natl Acad Sci U S A 1990;87:9868-72.
39. Ogawa S, Lee TM, Nayak AS, Glynn P. Oxygenation-sensitive contrast in magnetic resonance image of rodent brain at high magnetic fields. Magn Reson Med 1990;14:68-78.
40. Kwong KK, Belliveau JW, Chesler DA, Goldberg IE, Weisskoff RM, Poncelet BP, Kennedy DN, Hoppel BE, Cohen MS, Turner R. Dynamic magnetic resonance imaging of human brain activity during primary sensory stimulation. Proc Natl Acad Sci U S A 1992;89:5675-9.
41. Stüber C, Morawski M, Schäfer A, Labadie C, Wähnert M, Leuze C, Streicher M, Barapatre N, Reimann K, Geyer S, Spemann D, Turner R. Myelin and iron concentration in the human brain: a quantitative study of MRI contrast. Neuroimage 2014;93 Pt 1:95-106.
42. Lema Dopico A, Choi S, Hua J, Li X, Harrison DM. Multi-layer analysis of quantitative 7 T magnetic resonance imaging in the cortex of multiple sclerosis patients reveals pathology associated with disability. Mult Scler 2021;27:2040-51.
43. Duyn JH, van Gelderen P, Li TQ, de Zwart JA, Koretsky AP, Fukunaga M. High-field MRI of brain cortical substructure based on signal phase. Proc Natl Acad Sci U S A 2007;104:11796-801.
44. Fukunaga M, Li TQ, van Gelderen P, de Zwart JA, Shmueli K, Yao B, Lee J, Maric D, Aronova MA, Zhang G, Leapman RD, Schenck JF, Merkle H, Duyn JH. Layer-specific variation of iron content in cerebral cortex as a source of MRI contrast. Proc Natl Acad Sci U S A 2010;107:3834-9.
45. McColgan P, Helbling S, Vaculčiaková L, Pine K, Wagstyl K, Attar FM, Edwards L, Papoutsi M, Wei Y, Van den Heuvel MP, Tabrizi SJ, Rees G, Weiskopf N. Relating quantitative 7T MRI across cortical depths to cytoarchitectonics, gene expression and connectomics. Hum Brain Mapp 2021;42:4996-5009.
46. van Veluw SJ, Jolink WM, Hendrikse J, Geerlings MI, Luijten PR, Biessels GJ, Klijn CJ. Cortical microinfarcts on 7T MRI in patients with spontaneous intracerebral hemorrhage. J Cereb Blood Flow Metab 2014;34:1104-6.
47. Charidimou A. Convexity subarachnoid hemorrhage in cerebral amyloid angiopathy: the saga continues. J Cereb Blood Flow Metab 2015;35:707-9.
48. van Veluw SJ, Zwanenburg JJ, Engelen-Lee J, Spliet WG, Hendrikse J, Luijten PR, Biessels GJ. In vivo detection of cerebral cortical microinfarcts with high-resolution 7T MRI. J Cereb Blood Flow Metab 2013;33:322-9.
49. van Rooden S, Goos JD, van Opstal AM, Versluis MJ, Webb AG, Blauw GJ, van der Flier WM, Scheltens P, Barkhof F, van Buchem MA, van der Grond J. Increased number of microinfarcts in Alzheimer disease at 7-T MR imaging. Radiology 2014;270:205-11.
50. Summers PM, Hartmann DA, Hui ES, Nie X, Deardorff RL, McKinnon ET, Helpern JA, Jensen JH, Shih AY. Functional deficits induced by cortical microinfarcts. J Cereb Blood Flow Metab 2017;37:3599-614.
51. van Veluw SJ, Shih AY, Smith EE, Chen C, Schneider JA, Wardlaw JM, Greenberg SM, Biessels GJ. Detection, risk factors, and functional consequences of cerebral microinfarcts. Lancet Neurol 2017;16:730-40.
52. Doan NT, van Rooden S, Versluis MJ, Buijs M, Webb AG, van der Grond J, van Buchem MA, Reiber JHC, Milles J. An automated tool for cortical feature analysis: Application to differences on 7 Tesla T2* -weighted images between young and older healthy subjects. Magn Reson Med 2015;74:240-8.
53. van Rooden S, Doan NT, Versluis MJ, Goos JD, Webb AG, Oleksik AM, van der Flier WM, Scheltens P, Barkhof F, Weverling-Rynsburger AW, Blauw GJ, Reiber JH, van Buchem MA, Milles J, van der Grond J. 7T T *-weighted magnetic resonance imaging reveals cortical phase differences between early- and late-onset Alzheimer's disease. Neurobiol Aging 2015;36:20-6.
54. Nakada T, Matsuzawa H, Igarashi H, Fujii Y, Kwee IL. In vivo visualization of senile-plaque-like pathology in Alzheimer's disease patients by MR microscopy on a 7T system. J Neuroimaging 2008;18:125-9.
55. Tuzzi E, Balla DZ, Loureiro JRA, Neumann M, Laske C, Pohmann R, Preische O, Scheffler K, Hagberg GE. Ultra-High Field MRI in Alzheimer's Disease: Effective Transverse Relaxation Rate and Quantitative Susceptibility Mapping of Human Brain In Vivo and Ex Vivo compared to Histology. J Alzheimers Dis 2020;73:1481-99.
56. Geurts JJ, Pouwels PJ, Uitdehaag BM, Polman CH, Barkhof F, Castelijns JA. Intracortical lesions in multiple sclerosis: improved detection with 3D double inversion-recovery MR imaging. Radiology 2005;236:254-60.
57. Simon B, Schmidt S, Lukas C, Gieseke J, Träber F, Knol DL, Willinek WA, Geurts JJ, Schild HH, Barkhof F, Wattjes MP. Improved in vivo detection of cortical lesions in multiple sclerosis using double inversion recovery MR imaging at 3 Tesla. Eur Radiol 2010;20:1675-83.
58. Morimoto E, Kanagaki M, Okada T, Yamamoto A, Mori N, Matsumoto R, Ikeda A, Mikuni N, Kunieda T,

Paul D, Miyamoto S, Takahashi R, Togashi K. Anterior temporal lobe white matter abnormal signal (ATLAS) as an indicator of seizure focus laterality in temporal lobe epilepsy: comparison of double inversion recovery, FLAIR and T2W MR imaging. Eur Radiol 2013;23:3-11.
59. Morimoto E, Okada T, Kanagaki M, Yamamoto A, Fushimi Y, Matsumoto R, Takaya S, Ikeda A, Kunieda T, Kikuchi T, Paul D, Miyamoto S, Takahashi R, Togashi K. Evaluation of focus laterality in temporal lobe epilepsy: a quantitative study comparing double inversion-recovery MR imaging at 3T with FDG-PET. Epilepsia 2013;54:2174-83.
60. Tallantyre EC, Morgan PS, Dixon JE, Al-Radaideh A, Brookes MJ, Morris PG, Evangelou N. 3 Tesla and 7 Tesla MRI of multiple sclerosis cortical lesions. J Magn Reson Imaging 2010;32:971-7.
61. de Graaf WL, Zwanenburg JJ, Visser F, Wattjes MP, Pouwels PJ, Geurts JJ, Polman CH, Barkhof F, Luijten PR, Castelijns JA. Lesion detection at seven Tesla in multiple sclerosis using magnetisation prepared 3D-FLAIR and 3D-DIR. Eur Radiol 2012;22:221-31.
62. Pracht ED, Feiweier T, Ehses P, Brenner D, Roebroeck A, Weber B, Stöcker T. SAR and scan-time optimized 3D whole-brain double inversion recovery imaging at 7T. Magn Reson Med 2018;79:2620-8.
63. Urushibata Y, Kuribayashi H, Fujimoto K, Kober T, Grinstead JW, Isa T, Okada T. Advantages of fluid and white matter suppression (FLAWS) with MP2RAGE compared with double inversion recovery turbo spin echo (DIR-TSE) at 7T. Eur J Radiol 2019;116:160-4.
64. Tanner M, Gambarota G, Kober T, Krueger G, Erritzoe D, Marques JP, Newbould R. Fluid and white matter suppression with the MP2RAGE sequence. J Magn Reson Imaging 2012;35:1063-70.
65. Blinder P, Tsai PS, Kaufhold JP, Knutsen PM, Suhl H, Kleinfeld D. The cortical angiome: an interconnected vascular network with noncolumnar patterns of blood flow. Nat Neurosci 2013;16:889-97.
66. Wang L, Zhang Z, Okada T, Li C, Chen D, Funahashi S, Wu J, Yan T. Population Receptive Field Characteristics in the between- and Within-Digit Dimensions of the Undominant Hand in the Primary Somatosensory Cortex. Cereb Cortex 2021;31:4427-38.
67. Havlicek M, Uludağ K. A dynamical model of the laminar BOLD response. Neuroimage 2020;204:116209.
68. Marquardt I, Schneider M, Gulban OF, Ivanov D, Uludağ K. Cortical depth profiles of luminance contrast responses in human V1 and V2 using 7 T fMRI. Hum Brain Mapp 2018;39:2812-27.
69. Hua J, Qin Q, Donahue MJ, Zhou J, Pekar JJ, van Zijl PC. Inflow-based vascular-space-occupancy (iVASO) MRI. Magn Reson Med 2011;66:40-56.
70. Huber L, Ivanov D, Krieger SN, Streicher MN, Mildner T, Poser BA, Möller HE, Turner R. Slab-selective, BOLD-corrected VASO at 7 Tesla provides measures of cerebral blood volume reactivity with high signal-to-noise ratio. Magn Reson Med 2014;72:137-48.
71. Huber L, Ivanov D, Handwerker DA, Marrett S, Guidi M, Uludağ K, Bandettini PA, Poser BA. Techniques for blood volume fMRI with VASO: From low-resolution mapping towards sub-millimeter layer-dependent applications. Neuroimage 2018;164:131-43.
72. Hua J, Jones CK, Qin Q, van Zijl PC. Implementation of vascular-space-occupancy MRI at 7T. Magn Reson Med 2013;69:1003-13.
73. Huber L, Goense J, Kennerley AJ, Trampel R, Guidi M, Reimer E, Ivanov D, Neef N, Gauthier CJ, Turner R, Möller HE. Cortical lamina-dependent blood volume changes in human brain at 7 T. Neuroimage 2015;107:23-33.
74. Finn ES, Huber L, Jangraw DC, Molfese PJ, Bandettini PA. Layer-dependent activity in human prefrontal cortex during working memory. Nat Neurosci 2019;22:1687-95.
75. Huber LR, Poser BA, Kaas AL, Fear EJ, Dresbach S, Berwick J, Goebel R, Turner R, Kennerley AJ. Validating layer-specific VASO across species. Neuroimage 2021;237:118195.
76. Cho ZH, Han JY, Hwang SI, Kim DS, Kim KN, Kim NB, Kim SJ, Chi JG, Park CW, Kim YB. Quantitative analysis of the hippocampus using images obtained from 7.0 T MRI. Neuroimage 2010;49:2134-40.
77. Suthana NA, Donix M, Wozny DR, Bazih A, Jones M, Heidemann RM, Trampel R, Ekstrom AD, Scharf M, Knowlton B, Turner R, Bookheimer SY. High-resolution 7T fMRI of Human Hippocampal Subfields during Associative Learning. J Cogn Neurosci 2015;27:1194-206.
78. Pardoe HR, Antony AR, Hetherington H, Bagić AI, Shepherd TM, Friedman D, Devinsky O, Pan J. High resolution automated labeling of the hippocampus and amygdala using a 3D convolutional neural network trained on whole brain 700 µm isotropic 7T MP2RAGE MRI. Hum Brain Mapp 2021;42:2089-98.
79. DeKraker J, Ferko KM, Lau JC, Köhler S, Khan AR. Unfolding the hippocampus: An intrinsic coordinate system for subfield segmentations and quantitative mapping. Neuroimage 2018;167:408-18.

80. van der Meer D, Rokicki J, Kaufmann T, Córdova-Palomera A, Moberget T, Alnæs D, et al. Brain scans from 21,297 individuals reveal the genetic architecture of hippocampal subfield volumes. Mol Psychiatry 2020;25:3053-65.
81. Zheng F, Cui D, Zhang L, Zhang S, Zhao Y, Liu X, Liu C, Li Z, Zhang D, Shi L, Liu Z, Hou K, Lu W, Yin T, Qiu J. The Volume of Hippocampal Subfields in Relation to Decline of Memory Recall Across the Adult Lifespan. Front Aging Neurosci 2018;10:320.
82. Carey D, Nolan H, Kenny RA, Meaney J. Dissociable age and memory relationships with hippocampal subfield volumes in vivo:Data from the Irish Longitudinal Study on Ageing (TILDA). Sci Rep 2019;9:10981.
83. Wisse LE, Biessels GJ, Heringa SM, Kuijf HJ, Koek DH, Luijten PR, Geerlings MI; Utrecht Vascular Cognitive Impairment (VCI) Study Group. Hippocampal subfield volumes at 7T in early Alzheimer's disease and normal aging. Neurobiol Aging 2014;35:2039-45.
84. Shah P, Bassett DS, Wisse LEM, Detre JA, Stein JM, Yushkevich PA, Shinohara RT, Elliott MA, Das SR, Davis KA. Structural and functional asymmetry of medial temporal subregions in unilateral temporal lobe epilepsy: A 7T MRI study. Hum Brain Mapp 2019;40:2390-8.
85. Voets NL, Hodgetts CJ, Sen A, Adcock JE, Emir U. Hippocampal MRS and subfield volumetry at 7T detects dysfunction not specific to seizure focus. Sci Rep 2017;7:16138.
86. Brown SSG, Rutland JW, Verma G, Feldman RE, Alper J, Schneider M, Delman BN, Murrough JM, Balchandani P. Structural MRI at 7T reveals amygdala nuclei and hippocampal subfield volumetric association with Major Depressive Disorder symptom severity. Sci Rep 2019;9:10166.
87. Blom K, Koek HL, Zwartbol MHT, Ghaznawi R, Kuijf HJ, Witkamp TD, Hendrikse J, Biessels GJ, Geerlings MI; UCC-SMART Study Group. Vascular Risk Factors of Hippocampal Subfield Volumes in Persons without Dementia: The Medea 7T Study. J Alzheimers Dis 2020;77:1223-39.
88. Haast RAM, Lau JC, Ivanov D, Menon RS, Uludağ K, Khan AR. Effects of MP2RAGE B1+ sensitivity on inter-site T1 reproducibility and hippocampal morphometry at 7T. Neuroimage 2021;224:117373.
89. Haast RAM, Ivanov D, Uludağ K. The impact of B1+ correction on MP2RAGE cortical T1 and apparent cortical thickness at 7T. Hum Brain Mapp 2018;39:2412-25.
90. Forstmann BU, de Hollander G, van Maanen L, Alkemade A, Keuken MC. Towards a mechanistic understanding of the human subcortex. Nat Rev Neurosci 2016;18:57-65.
91. Deistung A, Schäfer A, Schweser F, Biedermann U, Turner R, Reichenbach JR. Toward in vivo histology: a comparison of quantitative susceptibility mapping (QSM) with magnitude-, phase-, and R2*-imaging at ultra-high magnetic field strength. Neuroimage 2013;65:299-314.
92. Keuken MC, Isaacs BR, Trampel R, van der Zwaag W, Forstmann BU. Visualizing the Human Subcortex Using Ultra-high Field Magnetic Resonance Imaging. Brain Topogr 2018;31:513-45.
93. Keuken MC, Bazin PL, Crown L, Hootsmans J, Laufer A, Müller-Axt C, Sier R, van der Putten EJ, Schäfer A, Turner R, Forstmann BU. Quantifying inter-individual anatomical variability in the subcortex using 7 T structural MRI. Neuroimage 2014;94:40-6.
94. Lenglet C, Abosch A, Yacoub E, De Martino F, Sapiro G, Harel N. Comprehensive in vivo mapping of the human basal ganglia and thalamic connectome in individuals using 7T MRI. PLoS One 2012;7:e29153.
95. Wang Y, Butros SR, Shuai X, Dai Y, Chen C, Liu M, Haacke EM, Hu J, Xu H. Different iron-deposition patterns of multiple system atrophy with predominant parkinsonism and idiopathetic Parkinson diseases demonstrated by phase-corrected susceptibility-weighted imaging. AJNR Am J Neuroradiol 2012;33:266-73.
96. Wallis LI, Paley MN, Graham JM, Grünewald RA, Wignall EL, Joy HM, Griffiths PD. MRI assessment of basal ganglia iron deposition in Parkinson's disease. J Magn Reson Imaging 2008;28:1061-7.
97. Gupta D, Saini J, Kesavadas C, Sarma PS, Kishore A. Utility of susceptibility-weighted MRI in differentiating Parkinson's disease and atypical parkinsonism. Neuroradiology 2010;52:1087-94.
98. Lee SH, Kim SS, Tae WS, Lee SY, Choi JW, Koh SB, Kwon DY. Regional volume analysis of the Parkinson disease brain in early disease stage: gray matter, white matter, striatum, and thalamus. AJNR Am J Neuroradiol 2011;32:682-7.
99. Barbagallo G, Sierra-Peña M, Nemmi F, Traon AP, Meissner WG, Rascol O, Péran P. Multimodal MRI assessment of nigro-striatal pathway in multiple system atrophy and Parkinson disease. Mov Disord 2016;31:325-34.
100. Lim SJ, Suh CH, Shim WH, Kim SJ. Diagnostic performance of T2* gradient echo, susceptibility-weighted imaging, and quantitative susceptibility mapping for

patients with multiple system atrophy-parkinsonian type: a systematic review and meta-analysis. Eur Radiol 2022;32:308-18.
101. Pang H, Yu Z, Li R, Yang H, Fan G. MRI-Based Radiomics of Basal Nuclei in Differentiating Idiopathic Parkinson's Disease From Parkinsonian Variants of Multiple System Atrophy: A Susceptibility-Weighted Imaging Study. Front Aging Neurosci 2020;12:587250.
102. Sjöström H, Granberg T, Westman E, Svenningsson P. Quantitative susceptibility mapping differentiates between parkinsonian disorders. Parkinsonism Relat Disord 2017;44:51-7.
103. Uchida Y, Kan H, Sakurai K, Inui S, Kobayashi S, Akagawa Y, Shibuya K, Ueki Y, Matsukawa N. Magnetic Susceptibility Associates With Dopaminergic Deficits and Cognition in Parkinson's Disease. Mov Disord 2020;35:1396-405.
104. van Bergen JM, Hua J, Unschuld PG, Lim IA, Jones CK, Margolis RL, Ross CA, van Zijl PC, Li X. Quantitative Susceptibility Mapping Suggests Altered Brain Iron in Premanifest Huntington Disease. AJNR Am J Neuroradiol 2016;37:789-96.
105. Puckett AM, Bollmann S, Poser BA, Palmer J, Barth M, Cunnington R. Using multi-echo simultaneous multi-slice (SMS) EPI to improve functional MRI of the subcortical nuclei of the basal ganglia at ultra-high field (7T). Neuroimage 2018;172:886-95.
106. Okun MS. Deep-brain stimulation for Parkinson's disease. N Engl J Med 2012;367:1529-38.
107. Ramirez-Zamora A, Ostrem JL. Globus Pallidus Interna or Subthalamic Nucleus Deep Brain Stimulation for Parkinson Disease: A Review. JAMA Neurol 2018;75:367-72.
108. Lozano AM, Dostrovsky J, Chen R, Ashby P. Deep brain stimulation for Parkinson's disease: disrupting the disruption. Lancet Neurol 2002;1:225-31.
109. Schaltenbrand G, Wahren W. Atlas for Stereotaxy of the Human Brain: Anatomical, Physiological and Clinical Applications. George Thieme Verlag, 1977.
110. Maruyama S, Fukunaga M, Fautz HP, Heidemann R, Sadato N. Comparison of 3T and 7T MRI for the visualization of globus pallidus sub-segments. Sci Rep 2019;9:18357.
111. Solomon O, Palnitkar T, Patriat R, Braun H, Aman J, Park MC, Vitek J, Sapiro G, Harel N. Deep-learning based fully automatic segmentation of the globus pallidus interna and externa using ultra-high 7 Tesla MRI. Hum Brain Mapp 2021;42:2862-79.
112. Hashimoto N, Ito YM, Okada N, Yamamori H, Yasuda Y, Fujimoto M, et al. The effect of duration of illness and antipsychotics on subcortical volumes in schizophrenia: Analysis of 778 subjects. Neuroimage Clin 2017;17:563-9.
113. Okamoto S, Sohn J, Tanaka T, Takahashi M, Ishida Y, Yamauchi K, Koike M, Fujiyama F, Hioki H. Overlapping Projections of Neighboring Direct and Indirect Pathway Neostriatal Neurons to Globus Pallidus External Segment. iScience 2020. [Epub ahead of print]. doi: 10.1016/j.isci.2020.101409.
114. Carrera E, Bogousslavsky J. The thalamus and behavior: effects of anatomically distinct strokes. Neurology 2006;66:1817-23.
115. Minagar A, Barnett MH, Benedict RH, Pelletier D, Pirko I, Sahraian MA, Frohman E, Zivadinov R. The thalamus and multiple sclerosis: modern views on pathologic, imaging, and clinical aspects. Neurology 2013;80:210-9.
116. Kipp M, Wagenknecht N, Beyer C, Samer S, Wuerfel J, Nikoubashman O. Thalamus pathology in multiple sclerosis: from biology to clinical application. Cell Mol Life Sci 2015;72:1127-47.
117. Capone F, Collorone S, Cortese R, Di Lazzaro V, Moccia M. Fatigue in multiple sclerosis: The role of thalamus. Mult Scler 2020;26:6-16.
118. Li MG, He JF, Liu XY, Wang ZF, Lou X, Ma L. Structural and Functional Thalamic Changes in Parkinson's Disease With Mild Cognitive Impairment. J Magn Reson Imaging 2020;52:1207-15.
119. Xiao Y, Zitella LM, Duchin Y, Teplitzky BA, Kastl D, Adriany G, Yacoub E, Harel N, Johnson MD. Multimodal 7T Imaging of Thalamic Nuclei for Preclinical Deep Brain Stimulation Applications. Front Neurosci 2016;10:264.
120. Johansen-Berg H, Behrens TE, Sillery E, Ciccarelli O, Thompson AJ, Smith SM, Matthews PM. Functional-anatomical validation and individual variation of diffusion tractography-based segmentation of the human thalamus. Cereb Cortex 2005;15:31-9.
121. Mang SC, Busza A, Reiterer S, Grodd W, Klose AU. Thalamus segmentation based on the local diffusion direction: a group study. Magn Reson Med 2012;67:118-26.
122. Calamante F, Tournier JD, Jackson GD, Connelly A. Track-density imaging (TDI): super-resolution white matter imaging using whole-brain track-density mapping. Neuroimage 2010;53:1233-43.
123. Calamante F, Tournier JD, Heidemann RM, Anwander A, Jackson GD, Connelly A. Track density imaging (TDI): validation of super resolution property. Neuroimage 2011;56:1259-66.
124. Kanowski M, Voges J, Buentjen L, Stadler J, Heinze HJ,

Tempelmann C. Direct visualization of anatomic subfields within the superior aspect of the human lateral thalamus by MRI at 7T. AJNR Am J Neuroradiol 2014;35:1721-7.
125. Traynor CR, Barker GJ, Crum WR, Williams SC, Richardson MP. Segmentation of the thalamus in MRI based on T1 and T2. Neuroimage 2011;56:939-50.
126. Tourdias T, Saranathan M, Levesque IR, Su J, Rutt BK. Visualization of intra-thalamic nuclei with optimized white-matter-nulled MPRAGE at 7T. Neuroimage 2014;84:534-45.
127. Datta R, Bacchus MK, Kumar D, Elliott MA, Rao A, Dolui S, Reddy R, Banwell BL, Saranathan M. Fast automatic segmentation of thalamic nuclei from MP2RAGE acquisition at 7 Tesla. Magn Reson Med 2021;85:2781-90.
128. Jorge J, Gretsch F, Najdenovska E, Tuleasca C, Levivier M, Maeder P, Gallichan D, Marques JP, Bach Cuadra M. Improved susceptibility-weighted imaging for high contrast and resolution thalamic nuclei mapping at 7T. Magn Reson Med 2020;84:1218-34.
129. Su JH, Thomas FT, Kasoff WS, Tourdias T, Choi EY, Rutt BK, Saranathan M. Thalamus Optimized Multi Atlas Segmentation (THOMAS): fast, fully automated segmentation of thalamic nuclei from structural MRI. Neuroimage 2019;194:272-82.
130. Hikosaka O. The habenula: from stress evasion to value-based decision-making. Nat Rev Neurosci 2010;11:503-13.
131. Schmidt FM, Schindler S, Adamidis M, Strauß M, Tränkner A, Trampel R, Walter M, Hegerl U, Turner R, Geyer S, Schönknecht P. Habenula volume increases with disease severity in unmedicated major depressive disorder as revealed by 7T MRI. Eur Arch Psychiatry Clin Neurosci 2017;267:107-15.
132. Strotmann B, Kögler C, Bazin PL, Weiss M, Villringer A, Turner R. Mapping of the internal structure of human habenula with ex vivo MRI at 7T. Front Hum Neurosci 2013;7:878.
133. Viswanath H, Carter AQ, Baldwin PR, Molfese DL, Salas R. The medial habenula: still neglected. Front Hum Neurosci 2014;7:931.
134. Matsumoto M, Hikosaka O. Lateral habenula as a source of negative reward signals in dopamine neurons. Nature 2007;447:1111-5.
135. Matsumoto M, Hikosaka O. Representation of negative motivational value in the primate lateral habenula. Nat Neurosci 2009;12:77-84.
136. Strotmann B, Heidemann RM, Anwander A, Weiss M, Trampel R, Villringer A, Turner R. High-resolution MRI and diffusion-weighted imaging of the human habenula at 7 tesla. J Magn Reson Imaging 2014;39:1018-26.
137. Kim JW, Naidich TP, Ely BA, Yacoub E, De Martino F, Fowkes ME, Goodman WK, Xu J. Human habenula segmentation using myelin content. Neuroimage 2016;130:145-56.
138. Abosch A, Yacoub E, Ugurbil K, Harel N. An assessment of current brain targets for deep brain stimulation surgery with susceptibility-weighted imaging at 7 tesla. Neurosurgery 2010;67:1745-56; discussion 1756.
139. Bronstein JM, Tagliati M, Alterman RL, Lozano AM, Volkmann J, Stefani A, et al. Deep brain stimulation for Parkinson disease: an expert consensus and review of key issues. Arch Neurol 2011;68:165.
140. Wong JK, Cauraugh JH, Ho KWD, Broderick M, Ramirez-Zamora A, Almeida L, Wagle Shukla A, Wilson CA, de Bie RM, Weaver FM, Kang N, Okun MS. STN vs. GPi deep brain stimulation for tremor suppression in Parkinson disease: A systematic review and meta-analysis. Parkinsonism Relat Disord 2019;58:56-62.
141. de Hollander G, Keuken MC, Bazin PL, Weiss M, Neumann J, Reimann K, Wähnert M, Turner R, Forstmann BU, Schäfer A. A gradual increase of iron toward the medial-inferior tip of the subthalamic nucleus. Hum Brain Mapp 2014;35:4440-9.
142. Keuken MC, Bazin PL, Schäfer A, Neumann J, Turner R, Forstmann BU. Ultra-high 7T MRI of structural age-related changes of the subthalamic nucleus. J Neurosci 2013;33:4896-900.
143. Kim S, Lee Y, Jeon CY, Kim K, Jeon Y, Jin YB, Oh S, Lee C. Quantitative magnetic susceptibility assessed by 7T magnetic resonance imaging in Alzheimer's disease caused by streptozotocin administration. Quant Imaging Med Surg 2020;10:789-97.
144. de Hollander G, Keuken MC, Forstmann BU. The subcortical cocktail problem; mixed signals from the subthalamic nucleus and substantia nigra. PLoS One 2015;10:e0120572.
145. de Hollander G, Keuken MC, van der Zwaag W, Forstmann BU, Trampel R. Comparing functional MRI protocols for small, iron-rich basal ganglia nuclei such as the subthalamic nucleus at 7 T and 3 T. Hum Brain Mapp 2017;38:3226-48.
146. Lehericy S, Vaillancourt DE, Seppi K, Monchi O, Rektorova I, Antonini A, McKeown MJ, Masellis M, Berg D, Rowe JB, Lewis SJG, Williams-Gray CH, Tessitore A, Siebner HR; International Parkinson and Movement Disorder Society (IPMDS)-Neuroimaging Study Group. The role of high-field magnetic resonance imaging in

parkinsonian disorders: Pushing the boundaries forward. Mov Disord 2017;32:510-25.
147. Sasaki M, Shibata E, Tohyama K, Takahashi J, Otsuka K, Tsuchiya K, Takahashi S, Ehara S, Terayama Y, Sakai A. Neuromelanin magnetic resonance imaging of locus ceruleus and substantia nigra in Parkinson's disease. Neuroreport 2006;17:1215-8.
148. Cassidy CM, Zucca FA, Girgis RR, Baker SC, Weinstein JJ, Sharp ME, Bellei C, Valmadre A, Vanegas N, Kegeles LS, Brucato G, Kang UJ, Sulzer D, Zecca L, Abi-Dargham A, Horga G. Neuromelanin-sensitive MRI as a noninvasive proxy measure of dopamine function in the human brain. Proc Natl Acad Sci U S A 2019;116:5108-17.
149. Ogisu K, Kudo K, Sasaki M, Sakushima K, Yabe I, Sasaki H, Terae S, Nakanishi M, Shirato H. 3D neuromelanin-sensitive magnetic resonance imaging with semi-automated volume measurement of the substantia nigra pars compacta for diagnosis of Parkinson's disease. Neuroradiology 2013;55:719-24.
150. Ohtsuka C, Sasaki M, Konno K, Kato K, Takahashi J, Yamashita F, Terayama Y. Differentiation of early-stage parkinsonisms using neuromelanin-sensitive magnetic resonance imaging. Parkinsonism Relat Disord 2014;20:755-60.
151. Sasaki M, Shibata E, Tohyama K, Kudo K, Endoh J, Otsuka K, Sakai A. Monoamine neurons in the human brain stem: anatomy, magnetic resonance imaging findings, and clinical implications. Neuroreport 2008;19:1649-54.
152. Oshima S, Fushimi Y, Okada T, Nakajima S, Yokota Y, Shima A, Grinstead J, Ahn S, Sawamoto N, Takahashi R, Nakamoto Y. Neuromelanin-Sensitive Magnetic Resonance Imaging Using DANTE Pulse. Mov Disord 2021;36:874-82.
153. Kwon DH, Kim JM, Oh SH, Jeong HJ, Park SY, Oh ES, Chi JG, Kim YB, Jeon BS, Cho ZH. Seven-Tesla magnetic resonance images of the substantia nigra in Parkinson disease. Ann Neurol 2012;71:267-77.
154. Duchin Y, Abosch A, Yacoub E, Sapiro G, Harel N. Feasibility of using ultra-high field (7 T) MRI for clinical surgical targeting. PLoS One 2012;7:e37328.
155. Cheng Z, He N, Huang P, Li Y, Tang R, Sethi SK, Ghassaban K, Yerramsetty KK, Palutla VK, Chen S, Yan F, Haacke EM. Imaging the Nigrosome 1 in the substantia nigra using susceptibility weighted imaging and quantitative susceptibility mapping: An application to Parkinson's disease. Neuroimage Clin 2020;25:102103.
156. Schwarz ST, Afzal M, Morgan PS, Bajaj N, Gowland PA, Auer DP. The 'swallow tail' appearance of the healthy nigrosome - a new accurate test of Parkinson's disease: a case-control and retrospective cross-sectional MRI study at 3T. PLoS One 2014;9:e93814.
157. De Marzi R, Seppi K, Högl B, Müller C, Scherfler C, Stefani A, Iranzo A, Tolosa E, Santamarìa J, Gizewski E, Schocke M, Skalla E, Kremser C, Poewe W. Loss of dorsolateral nigral hyperintensity on 3.0 tesla susceptibility-weighted imaging in idiopathic rapid eye movement sleep behavior disorder. Ann Neurol 2016;79:1026-30.
158. Mahlknecht P, Krismer F, Poewe W, Seppi K. Meta-analysis of dorsolateral nigral hyperintensity on magnetic resonance imaging as a marker for Parkinson's disease. Mov Disord 2017;32:619-23.
159. Mueller C, Pinter B, Reiter E, Schocke M, Scherfler C, Poewe W, Seppi K, Blazejewska AI, Schwarz ST, Bajaj N, Auer DP, Gowland PA. Visualization of nigrosome 1 and its loss in PD: pathoanatomical correlation and in vivo 7T MRI. Neurology 2014;82:1752.
160. Reiter E, Mueller C, Pinter B, Krismer F, Scherfler C, Esterhammer R, Kremser C, Schocke M, Wenning GK, Poewe W, Seppi K. Dorsolateral nigral hyperintensity on 3.0T susceptibility-weighted imaging in neurodegenerative Parkinsonism. Mov Disord 2015;30:1068-76.
161. Chau MT, Todd G, Wilcox R, Agzarian M, Bezak E. Diagnostic accuracy of the appearance of Nigrosome-1 on magnetic resonance imaging in Parkinson's disease: A systematic review and meta-analysis. Parkinsonism Relat Disord 2020;78:12-20.
162. Lehéricy S, Bardinet E, Poupon C, Vidailhet M, François C. 7 Tesla magnetic resonance imaging: a closer look at substantia nigra anatomy in Parkinson's disease. Mov Disord 2014;29:1574-81.
163. Schmidt MA, Engelhorn T, Marxreiter F, Winkler J, Lang S, Kloska S, Goelitz P, Doerfler A. Ultra high-field SWI of the substantia nigra at 7T: reliability and consistency of the swallow-tail sign. BMC Neurol 2017;17:194.
164. Gramsch C, Reuter I, Kraff O, Quick HH, Tanislav C, Roessler F, Deuschl C, Forsting M, Schlamann M. Nigrosome 1 visibility at susceptibility weighted 7T MRI-A dependable diagnostic marker for Parkinson's disease or merely an inconsistent, age-dependent imaging finding? PLoS One 2017;12:e0185489.
165. Kim JM, Jeong HJ, Bae YJ, Park SY, Kim E, Kang SY, Oh ES, Kim KJ, Jeon B, Kim SE, Cho ZH, Kim YB. Loss of substantia nigra hyperintensity on 7 Tesla MRI of Parkinson's disease, multiple system atrophy, and progressive supranuclear palsy. Parkinsonism Relat Disord

2016;26:47-54.
166. Le Bihan D, Mangin JF, Poupon C, Clark CA, Pappata S, Molko N, Chabriat H. Diffusion tensor imaging: concepts and applications. J Magn Reson Imaging 2001;13:534-46.
167. Tournier JD, Mori S, Leemans A. Diffusion tensor imaging and beyond. Magn Reson Med 2011;65:1532-56.
168. Wakana S, Jiang H, Nagae-Poetscher LM, van Zijl PC, Mori S. Fiber tract-based atlas of human white matter anatomy. Radiology 2004;230:77-87.
169. Chua TC, Wen W, Slavin MJ, Sachdev PS. Diffusion tensor imaging in mild cognitive impairment and Alzheimer's disease: a review. Curr Opin Neurol 2008;21:83-92.
170. Parente DB, Gasparetto EL, da Cruz LC Jr, Domingues RC, Baptista AC, Carvalho AC, Domingues RC. Potential role of diffusion tensor MRI in the differential diagnosis of mild cognitive impairment and Alzheimer's disease. AJR Am J Roentgenol 2008;190:1369-74.
171. Medina D, DeToledo-Morrell L, Urresta F, Gabrieli JD, Moseley M, Fleischman D, Bennett DA, Leurgans S, Turner DA, Stebbins GT. White matter changes in mild cognitive impairment and AD: A diffusion tensor imaging study. Neurobiol Aging 2006;27:663-72.
172. Huang J, Friedland RP, Auchus AP. Diffusion tensor imaging of normal-appearing white matter in mild cognitive impairment and early Alzheimer disease: preliminary evidence of axonal degeneration in the temporal lobe. AJNR Am J Neuroradiol 2007;28:1943-8.
173. Zhang Y, Wu IW, Buckley S, Coffey CS, Foster E, Mendick S, Seibyl J, Schuff N. Diffusion tensor imaging of the nigrostriatal fibers in Parkinson's disease. Mov Disord 2015;30:1229-36.
174. Theisen F, Leda R, Pozorski V, Oh JM, Adluru N, Wong R, Okonkwo O, Dean DC 3rd, Bendlin BB, Johnson SC, Alexander AL, Gallagher CL. Evaluation of striatonigral connectivity using probabilistic tractography in Parkinson's disease. Neuroimage Clin 2017;16:557-63.
175. Zhang Y, Burock MA. Diffusion Tensor Imaging in Parkinson's Disease and Parkinsonian Syndrome: A Systematic Review. Front Neurol 2020;11:531993. Erratum in: Front Neurol 2020 Oct 29;11:612069.
176. Kelly S, Jahanshad N, Zalesky A, Kochunov P, Agartz I, Alloza C, et al. Widespread white matter microstructural differences in schizophrenia across 4322 individuals: results from the ENIGMA Schizophrenia DTI Working Group. Mol Psychiatry 2018;23:1261-9.
177. van Velzen LS, Kelly S, Isaev D, Aleman A, Aftanas LI, Bauer J, et al. White matter disturbances in major depressive disorder: a coordinated analysis across 20 international cohorts in the ENIGMA MDD working group. Mol Psychiatry 2020;25:1511-25.
178. Cattarinussi G, Delvecchio G, Maggioni E, Bressi C, Brambilla P. Ultra-high field imaging in Major Depressive Disorder: a review of structural and functional studies. J Affect Disord 2021;290:65-73.
179. Favre P, Pauling M, Stout J, Hozer F, Sarrazin S, Abé C, et al. Widespread white matter microstructural abnormalities in bipolar disorder: evidence from mega- and meta-analyses across 3033 individuals. Neuropsychopharmacology 2019;44:2285-93. Erratum in: Neuropsychopharmacology. 2019 Dec;44(13):2298.
180. Kraus MF, Susmaras T, Caughlin BP, Walker CJ, Sweeney JA, Little DM. White matter integrity and cognition in chronic traumatic brain injury: a diffusion tensor imaging study. Brain 2007;130:2508-19.
181. Sidaros A, Engberg AW, Sidaros K, Liptrot MG, Herning M, Petersen P, Paulson OB, Jernigan TL, Rostrup E. Diffusion tensor imaging during recovery from severe traumatic brain injury and relation to clinical outcome: a longitudinal study. Brain 2008;131:559-72.
182. Polders DL, Leemans A, Hendrikse J, Donahue MJ, Luijten PR, Hoogduin JM. Signal to noise ratio and uncertainty in diffusion tensor imaging at 1.5, 3.0, and 7.0 Tesla. J Magn Reson Imaging 2011;33:1456-63.
183. Wasserthal J, Neher P, Maier-Hein KH. TractSeg - Fast and accurate white matter tract segmentation. Neuroimage 2018;183:239-53.
184. Skandsen T, Kvistad KA, Solheim O, Strand IH, Folvik M, Vik A. Prevalence and impact of diffuse axonal injury in patients with moderate and severe head injury: a cohort study of early magnetic resonance imaging findings and 1-year outcome. J Neurosurg 2010;113:556-63.
185. Hütter BO, Altmeppen J, Kraff O, Maderwald S, Theysohn JM, Ringelstein A, Wrede KH, Dammann P, Quick HH, Schlamann M, Moenninghoff C. Higher sensitivity for traumatic cerebral microbleeds at 7 T ultra-high field MRI: is it clinically significant for the acute state of the patients and later quality of life? Ther Adv Neurol Disord 2020;13:1756286420911295.
186. Lupo JM, Chuang CF, Chang SM, Barani IJ, Jimenez B, Hess CP, Nelson SJ. 7-Tesla susceptibility-weighted imaging to assess the effects of radiotherapy on normal-appearing brain in patients with glioma. Int J Radiat Oncol Biol Phys 2012;82:e493-500.
187. Morrison MA, Hess CP, Clarke JL, Butowski N, Chang SM, Molinaro AM, Lupo JM. Risk factors of radiotherapy-

induced cerebral microbleeds and serial analysis of their size compared with white matter changes: A 7T MRI study in 113 adult patients with brain tumors. J Magn Reson Imaging 2019;50:868-77.
188. Sepehry AA, Lang D, Hsiung GY, Rauscher A. Prevalence of Brain Microbleeds in Alzheimer Disease: A Systematic Review and Meta-Analysis on the Influence of Neuroimaging Techniques. AJNR Am J Neuroradiol 2016;37:215-22.
189. Dierksen GA, Skehan ME, Khan MA, Jeng J, Nandigam RN, Becker JA, Kumar A, Neal KL, Betensky RA, Frosch MP, Rosand J, Johnson KA, Viswanathan A, Salat DH, Greenberg SM. Spatial relation between microbleeds and amyloid deposits in amyloid angiopathy. Ann Neurol 2010;68:545-8.
190. Charidimou A, Farid K, Tsai HH, Tsai LK, Yen RF, Baron JC. Amyloid-PET burden and regional distribution in cerebral amyloid angiopathy: a systematic review and meta-analysis of biomarker performance. J Neurol Neurosurg Psychiatry 2018;89:410-7.
191. Farid K, Charidimou A, Baron JC. Amyloid positron emission tomography in sporadic cerebral amyloid angiopathy: A systematic critical update. Neuroimage Clin 2017;15:247-63.
192. Charidimou A, Meegahage R, Fox Z, Peeters A, Vandermeeren Y, Laloux P, Baron JC, Jäger HR, Werring DJ. Enlarged perivascular spaces as a marker of underlying arteriopathy in intracerebral haemorrhage: a multicentre MRI cohort study. J Neurol Neurosurg Psychiatry 2013;84:624-9.
193. Charidimou A, Jäger RH, Peeters A, Vandermeeren Y, Laloux P, Baron JC, Werring DJ. White matter perivascular spaces are related to cortical superficial siderosis in cerebral amyloid angiopathy. Stroke 2014;45:2930-5.
194. Bouvy WH, van Veluw SJ, Kuijf HJ, Zwanenburg JJ, Kappelle JL, Luijten PR, Koek HL, Geerlings MI, Biessels GJ; Utrecht Vascular Cognitive Impairment (VCI) Study Group. Microbleeds colocalize with enlarged juxtacortical perivascular spaces in amnestic mild cognitive impairment and early Alzheimer's disease: A 7 Tesla MRI study. J Cereb Blood Flow Metab 2020;40:739-46.
195. Barisano G, Law M, Custer RM, Toga AW, Sepehrband F. Perivascular Space Imaging at Ultrahigh Field MR Imaging. Magn Reson Imaging Clin N Am 2021;29:67-75.
196. Cai K, Tain R, Das S, Damen FC, Sui Y, Valyi-Nagy T, Elliott MA, Zhou XJ. The feasibility of quantitative MRI of perivascular spaces at 7T. J Neurosci Methods 2015;256:151-6.
197. Taoka T, Naganawa S. Glymphatic imaging using MRI. J Magn Reson Imaging 2020;51:11-24.
198. Davoodi-Bojd E, Ding G, Zhang L, Li Q, Li L, Chopp M, Zhang Z, Jiang Q. Modeling glymphatic system of the brain using MRI. Neuroimage 2019;188:616-27.
199. Gaberel T, Gakuba C, Goulay R, Martinez De Lizarrondo S, Hanouz JL, Emery E, Touze E, Vivien D, Gauberti M. Impaired glymphatic perfusion after strokes revealed by contrast-enhanced MRI: a new target for fibrinolysis? Stroke 2014;45:3092-6.
200. Naganawa S, Taoka T. The Glymphatic System: A Review of the Challenges in Visualizing its Structure and Function with MR Imaging. Magn Reson Med Sci 2022;21:182-94.
201. Ringstad G, Vatnehol SAS, Eide PK. Glymphatic MRI in idiopathic normal pressure hydrocephalus. Brain 2017;140:2691-705.
202. Naganawa S, Nakane T, Kawai H, Taoka T. Gd-based Contrast Enhancement of the Perivascular Spaces in the Basal Ganglia. Magn Reson Med Sci 2017;16:61-5.
203. Naganawa S, Nakane T, Kawai H, Taoka T. Age Dependence of Gadolinium Leakage from the Cortical Veins into the Cerebrospinal Fluid Assessed with Whole Brain 3D-real Inversion Recovery MR Imaging. Magn Reson Med Sci 2019;18:163-9.
204. Naganawa S, Nakane T, Kawai H, Taoka T. Differences in Signal Intensity and Enhancement on MR Images of the Perivascular Spaces in the Basal Ganglia versus Those in White Matter. Magn Reson Med Sci 2018;17:301-7.
205. Iliff JJ, Wang M, Liao Y, Plogg BA, Peng W, Gundersen GA, Benveniste H, Vates GE, Deane R, Goldman SA, Nagelhus EA, Nedergaard M. A paravascular pathway facilitates CSF flow through the brain parenchyma and the clearance of interstitial solutes, including amyloid β. Sci Transl Med 2012;4:147ra111.
206. Nedergaard M. Neuroscience. Garbage truck of the brain. Science 2013;340:1529-30.
207. Wardlaw JM, Benveniste H, Nedergaard M, Zlokovic BV, Mestre H, Lee H, et al. Perivascular spaces in the brain: anatomy, physiology and pathology. Nat Rev Neurol 2020;16:137-53.
208. Rasmussen MK, Mestre H, Nedergaard M. The glymphatic pathway in neurological disorders. Lancet Neurol 2018;17:1016-24.
209. Naganawa S, Ito R, Taoka T, Yoshida T, Sone M. The Space between the Pial Sheath and the Cortical Venous Wall May Connect to the Meningeal Lymphatics. Magn Reson Med Sci 2020;19:1-4.

210. Taoka T, Masutani Y, Kawai H, Nakane T, Matsuoka K, Yasuno F, Kishimoto T, Naganawa S. Evaluation of glymphatic system activity with the diffusion MR technique: diffusion tensor image analysis along the perivascular space (DTI-ALPS) in Alzheimer's disease cases. Jpn J Radiol 2017;35:172-8.
211. Bouvy WH, Biessels GJ, Kuijf HJ, Kappelle LJ, Luijten PR, Zwanenburg JJ. Visualization of perivascular spaces and perforating arteries with 7 T magnetic resonance imaging. Invest Radiol 2014;49:307-13.
212. Gotoh K, Okada T, Satogami N, Yakami M, Takahashi JC, Yoshida K, Ishii A, Tanaka S, Miyamoto S, Togashi K. Evaluation of CT angiography for visualisation of the lenticulostriate artery: difference between normotensive and hypertensive patients. Br J Radiol 2012;85:e1004-8.
213. Gotoh K, Okada T, Miki Y, Ikedo M, Ninomiya A, Kamae T, Togashi K. Visualization of the lenticulostriate artery with flow-sensitive black-blood acquisition in comparison with time-of-flight MR angiography. J Magn Reson Imaging 2009;29:65-9.
214. Okuchi S, Okada T, Ihara M, Gotoh K, Kido A, Fujimoto K, Yamamoto A, Kanagaki M, Tanaka S, Takahashi R, Togashi K. Visualization of lenticulostriate arteries by flow-sensitive black-blood MR angiography on a 1.5 T MRI system: a comparative study between subjects with and without stroke. AJNR Am J Neuroradiol 2013;34:780-4.
215. Okuchi S, Okada T, Fujimoto K, Fushimi Y, Kido A, Yamamoto A, Kanagaki M, Dodo T, Mehemed TM, Miyazaki M, Zhou X, Togashi K. Visualization of lenticulostriate arteries at 3T: Optimization of slice-selective off-resonance sinc pulse-prepared TOF-MRA and its comparison with flow-sensitive black-blood MRA. Acad Radiol 2014;21:812-6.
216. Kang CK, Park CA, Lee H, Kim SH, Park CW, Kim YB, Cho ZH. Hypertension correlates with lenticulostriate arteries visualized by 7T magnetic resonance angiography. Hypertension 2009;54:1050-6.
217. Seo SW, Kang CK, Kim SH, Yoon DS, Liao W, Wörz S, Rohr K, Kim YB, Na DL, Cho ZH. Measurements of lenticulostriate arteries using 7T MRI: new imaging markers for subcortical vascular dementia. J Neurol Sci 2012;322:200-5.
218. Grochowski C, Krukow P, Jonak K, Stępniewski A, Wawrzycki K, Maciejewski R. The assessment of lenticulostriate arteries originating from middle cerebral artery using ultra high-field magnetic resonance time-of-flight angiography. J Clin Neurosci 2019;68:262-5.
219. Cho ZH, Kang CK, Han JY, Kim SH, Kim KN, Hong SM, Park CW, Kim YB. Observation of the lenticulostriate arteries in the human brain in vivo using 7.0T MR angiography. Stroke 2008;39:1604-6.
220. Kurabe S, Okamoto K, Suzuki K, Matsuzawa H, Watanabe M, Suzuki Y, Nakada T, Fujii Y. The Posterior Limb of the Internal Capsule as the Subcortical Transitional Zone of the Anterior and Posterior Circulations: Insights from Human 7T MRI. Cerebrovasc Dis 2016;41:256-64.
221. Suzuki T, Natori T, Sasaki M, Miyazawa H, Narumi S, Ito K, Kamada A, Yoshida M, Tsuda K, Yoshioka K, Terayama Y. Evaluating recanalization of relevant lenticulostriate arteries in acute ischemic stroke using high-resolution MRA at 7T. Int J Stroke 2021;16:1039-46.
222. Todate Y, Uwano I, Yashiro S, Chida A, Hasegawa Y, Oda T, Nagasawa K, Honma H, Sasaki M, Ishigaki Y. High Prevalence of Cerebral Small Vessel Disease on 7T Magnetic Resonance Imaging in Familial Hypercholesterolemia. J Atheroscler Thromb 2019;26:1045-53.
223. Miyazawa H, Natori T, Kameda H, Sasaki M, Ohba H, Narumi S, Ito K, Sato M, Suzuki T, Tsuda K, Yoshioka K, Terayama Y. Detecting lenticulostriate artery lesions in patients with acute ischemic stroke using high-resolution MRA at 7 T. Int J Stroke 2019;14:290-7.
224. Kawashima M, Noguchi T, Takase Y, Ootsuka T, Kido N, Matsushima T. Unilateral hemispheric proliferation of ivy sign on fluid-attenuated inversion recovery images in moyamoya disease correlates highly with ipsilateral hemispheric decrease of cerebrovascular reserve. AJNR Am J Neuroradiol 2009;30:1709-16.
225. Horie N, Morikawa M, Nozaki A, Hayashi K, Suyama K, Nagata I. "Brush Sign" on susceptibility-weighted MR imaging indicates the severity of moyamoya disease. AJNR Am J Neuroradiol 2011;32:1697-702.
226. Uwano I, Kameda H, Harada T, Kobayashi M, Yanagihara W, Setta K, Ogasawara K, Yoshioka K, Yamashita F, Mori F, Matsuda T, Sasaki M. Detection of impaired cerebrovascular reactivity in patients with chronic cerebral ischemia using whole-brain 7T MRA. J Stroke Cerebrovasc Dis 2020;29:105081.
227. Togao O, Obara M, Helle M, Yamashita K, Kikuchi K, Momosaka D, Kikuchi Y, Nishimura A, Arimura K, Wada T, Murazaki H, Iihara K, Van Cauteren M, Hiwatashi A. Vessel-selective 4D-MR angiography using super-selective pseudo-continuous arterial spin labeling may be a useful tool for assessing brain AVM hemodynamics. Eur Radiol 2020;30:6452-63.

228. Togao O, Hiwatashi A, Obara M, Yamashita K, Momosaka D, Nishimura A, Arimura K, Hata N, Yoshimoto K, Iihara K, Van Cauteren M, Honda H. 4D ASL-based MR angiography for visualization of distal arteries and leptomeningeal collateral vessels in moyamoya disease: a comparison of techniques. Eur Radiol 2018;28:4871-81.
229. Togao O, Hiwatashi A, Obara M, Yamashita K, Kikuchi K, Kamei R, Nishimura A, Arimura K, Yoshimoto K, Iihara K, Van Cauteren M, Honda H. Acceleration-selective Arterial Spin-labeling MR Angiography Used to Visualize Distal Cerebral Arteries and Collateral Vessels in Moyamoya Disease. Radiology 2018;286:611-21.
230. Ivanov D, Gardumi A, Haast RAM, Pfeuffer J, Poser BA, Uludağ K. Comparison of 3T and 7T ASL techniques for concurrent functional perfusion and BOLD studies. Neuroimage 2017;156:363-76.
231. Gardener AG, Jezzard P. Investigating white matter perfusion using optimal sampling strategy arterial spin labeling at 7 Tesla. Magn Reson Med 2015;73:2243-8.
232. Serrai H, Buch S, Oran O, Menon RS. Using variable-rate selective excitation (VERSE) radiofrequency pulses to reduce power deposition in pulsed arterial spin labeling sequence at 7 Tesla. Magn Reson Med 2020;83:645-52.
233. Kashyap S, Ivanov D, Havlicek M, Huber L, Poser BA, Uludağ K. Sub-millimetre resolution laminar fMRI using Arterial Spin Labelling in humans at 7 T. PLoS One 2021;16:e0250504.
234. Tong Y, Jezzard P, Okell TW, Clarke WT. Improving PCASL at ultra-high field using a VERSE-guided parallel transmission strategy. Magn Reson Med 2020;84:777-86.
235. Viessmann O, Li L, Benjamin P, Jezzard P. T2-Weighted intracranial vessel wall imaging at 7 Tesla using a DANTE-prepared variable flip angle turbo spin echo readout (DANTE-SPACE). Magn Reson Med 2017;77:655-63.
236. Tkác I, Andersen P, Adriany G, Merkle H, Ugurbil K, Gruetter R. In vivo 1H NMR spectroscopy of the human brain at 7 T. Magn Reson Med 2001;46:451-6.
237. Pradhan S, Bonekamp S, Gillen JS, Rowland LM, Wijtenburg SA, Edden RA, Barker PB. Comparison of single voxel brain MRS AT 3T and 7T using 32-channel head coils. Magn Reson Imaging 2015;33:1013-8.
238. Tkác I, Oz G, Adriany G, Uğurbil K, Gruetter R. In vivo 1H NMR spectroscopy of the human brain at high magnetic fields: metabolite quantification at 4T vs. 7T. Magn Reson Med 2009;62:868-79.
239. Okada T, Kuribayashi H, Kaiser LG, Urushibata Y, Salibi N, Seethamraju RT, Ahn S, Thuy DHD, Fujimoto K, Isa T. Repeatability of proton magnetic resonance spectroscopy of the brain at 7 T: effect of scan time on semi-localized by adiabatic selective refocusing and short-echo time stimulated echo acquisition mode scans and their comparison. Quant Imaging Med Surg 2021;11:9-20.
240. Völzke Y, Pracht ED, Hattingen E, Y Tse DH, Stöcker T. On the reproducibility of hippocampal MEGA-sLASER GABA MRS at 7T using an optimized analysis pipeline. MAGMA 2021;34:427-36.
241. Wijtenburg SA, Rowland LM, Oeltzschner G, Barker PB, Workman CI, Smith GS. Reproducibility of brain MRS in older healthy adults at 7T. NMR Biomed 2019;32:e4040.
242. Wijtenburg SA, Rowland LM, Edden RA, Barker PB. Reproducibility of brain spectroscopy at 7T using conventional localization and spectral editing techniques. J Magn Reson Imaging 2013;38:460-7.
243. Prinsen H, de Graaf RA, Mason GF, Pelletier D, Juchem C. Reproducibility measurement of glutathione, GABA, and glutamate: Towards in vivo neurochemical profiling of multiple sclerosis with MR spectroscopy at 7T. J Magn Reson Imaging 2017;45:187-98.
244. Terpstra M, Cheong I, Lyu T, Deelchand DK, Emir UE, Bednařík P, Eberly LE, Öz G. Test-retest reproducibility of neurochemical profiles with short-echo, single-voxel MR spectroscopy at 3T and 7T. Magn Reson Med 2016;76:1083-91.
245. Lally N, An L, Banerjee D, Niciu MJ, Luckenbaugh DA, Richards EM, Roiser JP, Shen J, Zarate CA Jr, Nugent AC. Reliability of 7T (1) H-MRS measured human prefrontal cortex glutamate, glutamine, and glutathione signals using an adapted echo time optimized PRESS sequence: A between- and within-sessions investigation. J Magn Reson Imaging 2016;43:88-98.
246. Shams Z, van der Kemp WJM, Emir U, Dankbaar JW, Snijders TJ, de Vos FYF, Klomp DWJ, Wijnen JP, Wiegers EC. Comparison of 2-Hydroxyglutarate Detection With sLASER and MEGA-sLASER at 7T. Front Neurol 2021;12:718423.
247. Gonen OM, Moffat BA, Desmond PM, Lui E, Kwan P, O'Brien TJ. Seven-tesla quantitative magnetic resonance spectroscopy of glutamate, γ-aminobutyric acid, and glutathione in the posterior cingulate cortex/precuneus in patients with epilepsy. Epilepsia 2020;61:2785-94.
248. Krysko KM, Bischof A, Nourbakhsh B, Henry RG, Revirajan N, Manguinao M, Nguyen K, Akula A, Li Y, Waubant E. A pilot study of oxidative pathways in MS fatigue: randomized trial of N-acetyl cysteine. Ann Clin Transl Neurol 2021;8:811-24.
249. Wijtenburg SA, Wang M, Korenic SA, Chen S, Barker

PB, Rowland LM. Metabolite Alterations in Adults With Schizophrenia, First Degree Relatives, and Healthy Controls: A Multi-Region 7T MRS Study. Front Psychiatry 2021;12:656459.
250. Wang AM, Pradhan S, Coughlin JM, Trivedi A, DuBois SL, Crawford JL, Sedlak TW, Nucifora FC Jr, Nestadt G, Nucifora LG, Schretlen DJ, Sawa A, Barker PB. Assessing Brain Metabolism With 7-T Proton Magnetic Resonance Spectroscopy in Patients With First-Episode Psychosis. JAMA Psychiatry 2019;76:314-23.
251. Dempster K, Jeon P, MacKinley M, Williamson P, Théberge J, Palaniyappan L. Early treatment response in first episode psychosis: a 7-T magnetic resonance spectroscopic study of glutathione and glutamate. Mol Psychiatry 2020;25:1640-50.
252. Kumar J, Liddle EB, Fernandes CC, Palaniyappan L, Hall EL, Robson SE, Simmonite M, Fiesal J, Katshu MZ, Qureshi A, Skelton M, Christodoulou NG, Brookes MJ, Morris PG, Liddle PF. Glutathione and glutamate in schizophrenia: a 7T MRS study. Mol Psychiatry 2020;25:873-82.
253. Song XM, Hu XW, Li Z, Gao Y, Ju X, Liu DY, Wang QN, Xue C, Cai YC, Bai R, Tan ZL, Northoff G. Reduction of higher-order occipital GABA and impaired visual perception in acute major depressive disorder. Mol Psychiatry 2021;26:6747-55.
254. Smith GS, Oeltzschner G, Gould NF, Leoutsakos JS, Nassery N, Joo JH, Kraut MA, Edden RAE, Barker PB, Wijtenburg SA, Rowland LM, Workman CI. Neurotransmitters and Neurometabolites in Late-Life Depression: A Preliminary Magnetic Resonance Spectroscopy Study at 7T. J Affect Disord 2021;279:417-25.
255. Puts NA, Ryan M, Oeltzschner G, Horska A, Edden RAE, Mahone EM. Reduced striatal GABA in unmedicated children with ADHD at 7T. Psychiatry Res Neuroimaging 2020;301:111082.
256. Park YW, Deelchand DK, Joers JM, Kumar A, Alvear AB, Moheet A, Seaquist ER, Öz G. Monitoring the Neurotransmitter Response to Glycemic Changes Using an Advanced Magnetic Resonance Spectroscopy Protocol at 7T. Front Neurol 2021;12:698675.
257. Ip IB, Berrington A, Hess AT, Parker AJ, Emir UE, Bridge H. Combined fMRI-MRS acquires simultaneous glutamate and BOLD-fMRI signals in the human brain. Neuroimage 2017;155:113-9.
258. Nassirpour S, Chang P, Henning A. High and ultra-high resolution metabolite mapping of the human brain using 1H FID MRSI at 9.4T. Neuroimage 2018;168:211-21.
259. Nassirpour S, Chang P, Henning A. MultiNet PyGRAPPA: Multiple neural networks for reconstructing variable density GRAPPA (a 1H FID MRSI study). Neuroimage 2018;183:336-45.
260. Heckova E, Strasser B, Hangel GJ, Považan M, Dal-Bianco A, Rommer PS, Bednarik P, Gruber S, Leutmezer F, Lassmann H, Trattnig S, Bogner W. 7 T Magnetic Resonance Spectroscopic Imaging in Multiple Sclerosis: How Does Spatial Resolution Affect the Detectability of Metabolic Changes in Brain Lesions? Invest Radiol 2019;54:247-54.
261. Hangel G, Jain S, Springer E, Hečková E, Strasser B, Považan M, Gruber S, Widhalm G, Kiesel B, Furtner J, Preusser M, Roetzer T, Trattnig S, Sima DM, Smeets D, Bogner W. High-resolution metabolic mapping of gliomas via patch-based super-resolution magnetic resonance spectroscopic imaging at 7T. Neuroimage 2019;191:587-95.
262. van Veenendaal TM, Backes WH, Tse DHY, Scheenen TWJ, Klomp DW, Hofman PAM, Rouhl RPW, Vlooswijk MCG, Aldenkamp AP, Jansen JFA. High field imaging of large-scale neurotransmitter networks: Proof of concept and initial application to epilepsy. Neuroimage Clin 2018;19:47-55.
263. Mescher M, Merkle H, Kirsch J, Garwood M, Gruetter R. Simultaneous in vivo spectral editing and water suppression. NMR Biomed 1998;11:266-72.
264. Mikkelsen M, Barker PB, Bhattacharyya PK, Brix MK, Buur PF, Cecil KM, et al. Big GABA: Edited MR spectroscopy at 24 research sites. Neuroimage 2017;159:32-45.
265. Považan M, Strasser B, Hangel G, Heckova E, Gruber S, Trattnig S, Bogner W. Simultaneous mapping of metabolites and individual macromolecular components via ultra-short acquisition delay 1 H MRSI in the brain at 7T. Magn Reson Med 2018;79:1231-40.
266. Považan M, Hangel G, Strasser B, Gruber S, Chmelik M, Trattnig S, Bogner W. Mapping of brain macromolecules and their use for spectral processing of (1)H-MRSI data with an ultra-short acquisition delay at 7 T. Neuroimage 2015;121:126-35.
267. Ward KM, Aletras AH, Balaban RS. A new class of contrast agents for MRI based on proton chemical exchange dependent saturation transfer (CEST). J Magn Reson 2000;143:79-87.
268. van Zijl PC, Yadav NN. Chemical exchange saturation transfer (CEST): what is in a name and what isn't? Magn Reson Med 2011;65:927-48.
269. Dou W, Lin CE, Ding H, Shen Y, Dou C, Qian L, Wen

B, Wu B. Chemical exchange saturation transfer magnetic resonance imaging and its main and potential applications in pre-clinical and clinical studies. Quant Imaging Med Surg 2019;9:1747-66.
270. Kamimura K, Nakajo M, Yoneyama T, Fukukura Y, Hirano H, Goto Y, Sasaki M, Akamine Y, Keupp J, Yoshiura T. Histogram analysis of amide proton transfer-weighted imaging: comparison of glioblastoma and solitary brain metastasis in enhancing tumors and peritumoral regions. Eur Radiol 2019;29:4133-40.
271. Zhou J, Wilson DA, Sun PZ, Klaus JA, Van Zijl PC. Quantitative description of proton exchange processes between water and endogenous and exogenous agents for WEX, CEST, and APT experiments. Magn Reson Med 2004;51:945-52.
272. Sagiyama K, Mashimo T, Togao O, Vemireddy V, Hatanpaa KJ, Maher EA, Mickey BE, Pan E, Sherry AD, Bachoo RM, Takahashi M. In vivo chemical exchange saturation transfer imaging allows early detection of a therapeutic response in glioblastoma. Proc Natl Acad Sci U S A 2014;111:4542-7.
273. Togao O, Hiwatashi A, Yamashita K, Kikuchi K, Mizoguchi M, Yoshimoto K, Suzuki SO, Iwaki T, Obara M, Van Cauteren M, Honda H. Differentiation of high-grade and low-grade diffuse gliomas by intravoxel incoherent motion MR imaging. Neuro Oncol 2016;18:132-41.
274. Togao O, Yoshiura T, Keupp J, Hiwatashi A, Yamashita K, Kikuchi K, Suzuki Y, Suzuki SO, Iwaki T, Hata N, Mizoguchi M, Yoshimoto K, Sagiyama K, Takahashi M, Honda H. Amide proton transfer imaging of adult diffuse gliomas: correlation with histopathological grades. Neuro Oncol 2014;16:441-8.
275. Sakata A, Okada T, Yamamoto Y, Fushimi Y, Dodo T, Arakawa Y, Mineharu Y, Schmitt B, Miyamoto S, Togashi K. Addition of Amide Proton Transfer Imaging to FDG-PET/CT Improves Diagnostic Accuracy in Glioma Grading: A Preliminary Study Using the Continuous Net Reclassification Analysis. AJNR Am J Neuroradiol 2018;39:265-72.
276. Sakata A, Fushimi Y, Okada T, Arakawa Y, Kunieda T, Minamiguchi S, Kido A, Sakashita N, Miyamoto S, Togashi K. Diagnostic performance between contrast enhancement, proton MR spectroscopy, and amide proton transfer imaging in patients with brain tumors. J Magn Reson Imaging 2017;46:732-9.
277. Sakata A, Okada T, Yamamoto A, Kanagaki M, Fushimi Y, Okada T, Dodo T, Arakawa Y, Schmitt B, Miyamoto S, Togashi K. Grading glial tumors with amide proton transfer MR imaging: different analytical approaches. J Neurooncol 2015;122:339-48.
278. Zaiss M, Windschuh J, Goerke S, Paech D, Meissner JE, Burth S, Kickingereder P, Wick W, Bendszus M, Schlemmer HP, Ladd ME, Bachert P, Radbruch A. Downfield-NOE-suppressed amide-CEST-MRI at 7 Tesla provides a unique contrast in human glioblastoma. Magn Reson Med 2017;77:196-208.
279. Paech D, Zaiss M, Meissner JE, Windschuh J, Wiestler B, Bachert P, Neumann JO, Kickingereder P, Schlemmer HP, Wick W, Nagel AM, Heiland S, Ladd ME, Bendszus M, Radbruch A. Nuclear overhauser enhancement mediated chemical exchange saturation transfer imaging at 7 Tesla in glioblastoma patients. PLoS One 2014;9:e104181.
280. Paech D, Windschuh J, Oberhollenzer J, Dreher C, Sahm F, Meissner JE, Goerke S, Schuenke P, Zaiss M, Regnery S, Bickelhaupt S, Bäumer P, Bendszus M, Wick W, Unterberg A, Bachert P, Ladd ME, Schlemmer HP, Radbruch A. Assessing the predictability of IDH mutation and MGMT methylation status in glioma patients using relaxation-compensated multipool CEST MRI at 7.0 T. Neuro Oncol 2018;20:1661-71.
281. Cai K, Haris M, Singh A, Kogan F, Greenberg JH, Hariharan H, Detre JA, Reddy R. Magnetic resonance imaging of glutamate. Nat Med 2012;18:302-6.
282. Davis KA, Nanga RP, Das S, Chen SH, Hadar PN, Pollard JR, Lucas TH, Shinohara RT, Litt B, Hariharan H, Elliott MA, Detre JA, Reddy R. Glutamate imaging (GluCEST) lateralizes epileptic foci in nonlesional temporal lobe epilepsy. Sci Transl Med 2015;7:309ra161.
283. Hadar PN, Kini LG, Nanga RPR, Shinohara RT, Chen SH, Shah P, Wisse LEM, Elliott MA, Hariharan H, Reddy R, Detre JA, Stein JM, Das S, Davis KA. Volumetric glutamate imaging (GluCEST) using 7T MRI can lateralize nonlesional temporal lobe epilepsy: A preliminary study. Brain Behav 2021;11:e02134.
284. Roalf DR, Nanga RPR, Rupert PE, Hariharan H, Quarmley M, Calkins ME, Dress E, Prabhakaran K, Elliott MA, Moberg PJ, Gur RC, Gur RE, Reddy R, Turetsky BI. Glutamate imaging (GluCEST) reveals lower brain GluCEST contrast in patients on the psychosis spectrum. Mol Psychiatry 2017;22:1298-305.
285. Vaughan JT, Garwood M, Collins CM, Liu W, DelaBarre L, Adriany G, Andersen P, Merkle H, Goebel R, Smith MB, Ugurbil K. 7T vs. 4T: RF power, homogeneity, and signal-to-noise comparison in head images. Magn Reson Med 2001;46:24-30.
286. Yamamoto T, Fukunaga M, Sugawara SK, Hamano YH,

Sadato N. Quantitative Evaluations of Geometrical Distortion Corrections in Cortical Surface-Based Analysis of High-Resolution Functional MRI Data at 7T. J Magn Reson Imaging 2021;53:1220-34.
287. Barmet C, De Zanche N, Wilm BJ, Pruessmann KP. A transmit/receive system for magnetic field monitoring of in vivo MRI. Magn Reson Med 2009;62:269-76.
288. Wyss M, Duerst Y, Nanz D, Kasper L, Wilm BJ, Dietrich BE, Gross S, Schmid T, Brunner DO, Pruessmann KP. Feedback field control improves the precision of T2 * quantification at 7 T. NMR Biomed 2017.
289. Mattern H, Sciarra A, Godenschweger F, Stucht D, Lüsebrink F, Rose G, Speck O. Prospective motion correction enables highest resolution time-of-flight angiography at 7T. Magn Reson Med 2018;80:248-58.
290. Özbay PS, Duerst Y, Wilm BJ, Pruessmann KP, Nanz D. Enhanced quantitative susceptibility mapping (QSM) using real-time field control. Magn Reson Med 2018;79:770-8.
291. Mattern H, Sciarra A, Lüsebrink F, Acosta-Cabronero J, Speck O. Prospective motion correction improves high-resolution quantitative susceptibility mapping at 7T. Magn Reson Med 2019;81:1605-19.
292. Federau C, Gallichan D. Motion-Correction Enabled Ultra-High Resolution In-Vivo 7T-MRI of the Brain. PLoS One 2016;11:e0154974.
293. Bian W, Kerr AB, Tranvinh E, Parivash S, Zahneisen B, Han MH, Lock CB, Goubran M, Zhu K, Rutt BK, Zeineh MM. MR susceptibility contrast imaging using a 2D simultaneous multi-slice gradient-echo sequence at 7T. PLoS One 2019;14:e0219705.
294. Vaidya MV, Lazar M, Deniz CM, Haemer GG, Chen G, Bruno M, Sodickson DK, Lattanzi R, Collins CM. Improved detection of fMRI activation in the cerebellum at 7T with dielectric pads extending the imaging region of a commercial head coil. J Magn Reson Imaging 2018;48:431-40.
295. Haast RA, Ivanov D, Formisano E, Uludağ K. Reproducibility and Reliability of Quantitative and Weighted T1 and T2* Mapping for Myelin-Based Cortical Parcellation at 7 Tesla. Front Neuroanat 2016;10:112.
296. Seiger R, Hahn A, Hummer A, Kranz GS, Ganger S, Küblböck M, Kraus C, Sladky R, Kasper S, Windischberger C, Lanzenberger R. Voxel-based morphometry at ultra-high fields. a comparison of 7T and 3T MRI data. Neuroimage 2015;113:207-16.
297. Eggenschwiler F, Kober T, Magill AW, Gruetter R, Marques JP. SA2RAGE: a new sequence for fast B1+ -mapping. Magn Reson Med 2012;67:1609-19.
298. Oran OF, Klassen LM, Gilbert KM, Gati JS, Menon RS. Elimination of low-inversion-efficiency induced artifacts in whole-brain MP2RAGE using multiple RF-shim configurations at 7 T. NMR Biomed 2020;33:e4387.
299. Wu X, Auerbach EJ, Vu AT, Moeller S, Lenglet C, Schmitter S, Van de Moortele PF, Yacoub E, Uğurbil K. High-resolution whole-brain diffusion MRI at 7T using radiofrequency parallel transmission. Magn Reson Med 2018;80:1857-70.
300. Wu X, Auerbach EJ, Vu AT, Moeller S, Van de Moortele PF, Yacoub E, Uğurbil K. Human Connectome Project-style resting-state functional MRI at 7 Tesla using radiofrequency parallel transmission. Neuroimage 2019;184:396-408.
301. Massire A, Vignaud A, Robert B, Le Bihan D, Boulant N, Amadon A. Parallel-transmission-enabled three-dimensional T2 -weighted imaging of the human brain at 7 Tesla. Magn Reson Med 2015;73:2195-203.
302. Kopanoglu E, Deniz CM, Erturk MA, Wise RG. Specific absorption rate implications of within-scan patient head motion for ultra-high field MRI. Magn Reson Med 2020;84:2724-38.
303. Cloos MA, Boulant N, Luong M, Ferrand G, Giacomini E, Le Bihan D, Amadon A. kT -points: short three-dimensional tailored RF pulses for flip-angle homogenization over an extended volume. Magn Reson Med 2012;67:72-80.
304. Eggenschwiler F, O'Brien KR, Gallichan D, Gruetter R, Marques JP. 3D T 2-weighted imaging at 7T using dynamic kT-points on single-transmit MRI systems. MAGMA 2016;29:347-58.
305. Gras V, Vignaud A, Amadon A, Le Bihan D, Boulant N. Universal pulses: A new concept for calibration-free parallel transmission. Magn Reson Med 2017;77:635-43.
306. Le Garrec M, Gras V, Hang MF, Ferrand G, Luong M, Boulant N. Probabilistic analysis of the specific absorption rate intersubject variability safety factor in parallel transmission MRI. Magn Reson Med 2017;78:1217-23.
307. Gras V, Poser BA, Wu X, Tomi-Tricot R, Boulant N. Optimizing BOLD sensitivity in the 7T Human Connectome Project resting-state fMRI protocol using plug-and-play parallel transmission. Neuroimage 2019;195:1-10.
308. Gras V, Mauconduit F, Vignaud A, Amadon A, Le Bihan D, Stöcker T, Boulant N. Design of universal parallel-transmit refocusing kT -point pulses and application to 3D T2 -weighted imaging at 7T. Magn Reson Med 2018;80:53-65.

309. Eggenschwiler F, O'Brien KR, Gruetter R, Marques JP. Improving T2 -weighted imaging at high field through the use of kT -points. Magn Reson Med 2014;71:1478-88.
310. Tomi-Tricot R, Gras V, Thirion B, Mauconduit F, Boulant N, Cherkaoui H, Zerbib P, Vignaud A, Luciani A, Amadon A. SmartPulse, a machine learning approach for calibration-free dynamic RF shimming: Preliminary study in a clinical environment. Magn Reson Med 2019;82:2016-31.
311. Okada T, Handa S, Ding B, Urayama SI, Fujimoto K, Shima A, Yoshii D, Ayaki T, Sawamoto N, Takahashi R, Onoe H, Isa T, Petropoulos L. Insertable inductively coupled volumetric coils for MR microscopy in a human 7T MR system. Magn Reson Med 2022;87:1613-20.
312. McKiernan EF, O'Brien JT. 7T MRI for neurodegenerative dementias in vivo: a systematic review of the literature. J Neurol Neurosurg Psychiatry 2017;88:564-74.
313. Düzel E, Acosta-Cabronero J, Berron D, Biessels GJ, Björkman-Burtscher I, Bottlaender M, et al. European Ultrahigh-Field Imaging Network for Neurodegenerative Diseases (EUFIND). Alzheimers Dement (Amst) 2019;11:538-49.

Cite this article as: Okada T, Fujimoto K, Fushimi Y, Akasaka T, Thuy DHD, Shima A, Sawamoto N, Oishi N, Zhang Z, Funaki T, Nakamoto Y, Murai T, Miyamoto S, Takahashi R, Isa T. Neuroimaging at 7 Tesla: a pictorial narrative review. Quant Imaging Med Surg 2022;12(6):3406-3435. doi: 10.21037/qims-21-969

